IOP Publishing Classical and Quantum Gravity
Class. Quantum Grav. **39** (2022) 025008 (33pp) https://doi.org/10.1088/1361-6382/ac2b08

Surface and underground seismic characterization at Terziet in Limburg—the Euregio Meuse–Rhine candidate site for Einstein Telescope

Soumen Koley[1,2,*], Maria Bader[2], Jo van den Brand[2,3], Xander Campman[4], Henk Jan Bulten[2,5], Frank Linde[2,6] and Bjorn Vink[7]

[1] Gran Sasso Science Institute (GSSI), I-67100 L'Aquila, Italy
[2] Nikhef, Science Park, 1098 XG Amsterdam, The Netherlands
[3] Maastricht University, 6211 LK Maastricht, The Netherlands
[4] Shell Global Solutions International BV, The Netherlands
[5] Vrije Universiteit Amsterdam, 1081 HV Amsterdam, The Netherlands
[6] University of Amsterdam, 1012 WX Amsterdam, The Netherlands
[7] Antea Group BV, The Netherlands

E-mail: soumen.koley@gssi.it

Received 1 June 2021, revised 2 September 2021
Accepted for publication 28 September 2021
Published 11 January 2022

Abstract

We present a detailed characterization of surface and underground seismic noise measured at Limburg in the south of the Netherlands. This location is the Euregio Meuse–Rhine candidate for hosting Einstein Telescope, a future observatory for gravitational waves. Seismic noise measurements were performed with an array of seismometers installed on the surface. Passive seismic methods like beamforming were used to extract the propagation wave types of ambient seismic noise and the Rayleigh-wave dispersion in the region. Subsurface shear-wave models sensitive to depths of 300 m were derived by using the Rayleigh-wave dispersion and ellipticity. Subsurface P-wave velocities to depths of 200 m were obtained from an active seismic survey. Wavepath Eikonal tomography was used on the source-receiver refracted-wave travel-times to obtain a subsurface P-wave velocity model. Both the passive and the active seismic data analysis point to the presence of a layered geology with a soft-soil to hard-rock transition occurring at a shallow depth of about 25 to 40 m. The surface arrays are complemented by two permanent tri-axial seismometers installed on the surface and in a borehole at 250 m depth. Their data are used to interpret the surface-wave and body-wave contributions to the observed seismic noise.

*Author to whom any correspondence should be addressed.

We use a cross-correlation analysis and compute the theoretical surface-wave eigenfunctions to understand the contributions of the different wave types at different frequencies. We observe that below 4 Hz in the horizontal component and 9 Hz in the vertical component, the seismic noise at depth is dominantly due to surface waves. Above these frequencies a significant contribution can be attributed to both nearby and far-away body-wave sources. At a depth of 250 m we find that the surface noise power has been damped by up to a factor 10^4 above about 2 Hz. The Limburg geology with soft-soil on top of hard-rock efficiently damps the anthropogenic noise produced at the surface. This implies that Einstein Telescope's test masses are shielded from anthropogenic seismic noise and construction at greater depth will not bring significant further improvements in this regard. A body-wave background has been identified that contributes about half of the total underground seismic noise at 250 m depth for frequencies above 4 Hz. It remains to be studied if subtraction schemes for Newtonian noise originating from this body-wave background will be necessary. Finally, we estimate an interferometer downtime of about 3% due to regional and teleseismic earthquakes. We believe this is acceptable as it is comparable to current experience at the LIGO and Virgo interferometer sites.

Keywords: ambient seismic noise, Einstein telescope, body wave background, underground seismic noise, Newtonian noise

(Some figures may appear in colour only in the online journal)

1. Introduction

The LIGO and Virgo ground-based gravitational-wave detectors have achieved sensitivities in the order of 10^{-23} strain$/\sqrt{\text{Hz}}$ for frequencies from about 50 to 10^3 Hz [1, 2]. Third generation observatories like Einstein Telescope [3] and Cosmic Explorer [4] aim at sensitivities that are about an order of magnitude improvement over current design sensitivities of LIGO and Virgo. Cosmic Explorer will be a surface-based gravitational wave observatory realized in the USA, while Einstein Telescope will be constructed underground in Europe in an attempt to obtain improved low-frequency sensitivity. Its observation band starts at 3 Hz and an improvement in sensitivity by more than three orders of magnitude over current detectors is foreseen at 10 Hz. This is a challenge, as thermal, seismic and Newtonian noise [5, 6] limit the low-frequency sensitivity. Apart from directly shaking the test-masses via the suspensions (seismic noise), the seismic displacement and density fluctuations of the surroundings couple to the suspended elements through gravitational forces and introduce noise to the interferometer output signal. This noise is referred to as Newtonian noise or gravity-gradient noise [7]. Besides seismic ground motion, atmospheric density fluctuations contribute to Newtonian noise [8]. In this paper we focus solely on the contribution of seismic motion to Newtonian noise.

The Advanced LIGO [9] and Advanced Virgo [10] detectors are built on the surface of the Earth. Sophisticated techniques in seismic isolation are applied on the suspended elements to reduce the seismic ground motion above a few Hz by about 12 orders of magnitude [11]. This approach of seismic attenuation is compatible with the sensitivity requirements of Einstein Telescope above frequencies of 4 Hz [12]. However, the coupling of Newtonian noise to the detector cannot be suppressed with passive shielding or improved suspensions.

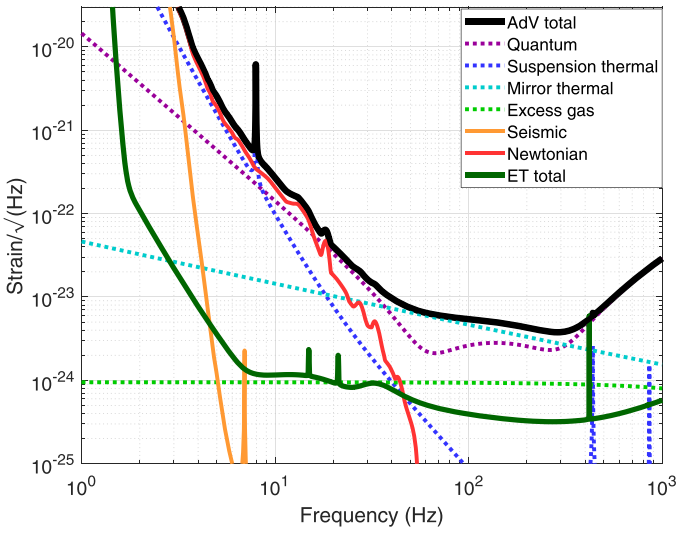

Figure 1. Design sensitivity of Einstein Telescope and the Advanced Virgo detector. The contributions of various noise sources to the sensitivity of Advanced Virgo are indicated. The sensitivity of Einstein Telescope would be limited by Newtonian noise below about 40 Hz if it were built on the Earth's surface in a Virgo-like seismic noise environment. Note that the Newtonian noise contribution for Einstein Telescope between 2 and 6 Hz was calculated from the horizontal displacement spectrum measured at night-time at the underground seismic facility of the Black Forest Observatory [6]. The corresponding power spectral density (PSD) was assumed to be homogeneous and is about two orders of magnitude smaller than that observed at the Advanced Virgo site.

The contribution of the different noise sources to the total noise budget of Advanced Virgo is shown in figure 1 [10]. The figure also shows the design sensitivity of Einstein Telescope [3]. We can infer that if Einstein Telescope were to be built on the surface, its sensitivity would be severely limited below about 40 Hz by Newtonian noise. Hence, our quest for unprecedented low-frequency sensitivity motivates building Einstein Telescope underground and at a site with minimal surface seismic noise [13]. The ideal site would effectively attenuate seismic noise generated at the surface and would have low levels of ambient background noise.

Modeling of Newtonian noise requires the computation of the displacement or deformation of individual subsurface elements in the vicinity of the test-masses (i.e. near the main mirrors of the interferometer). Subsurface displacements can be calculated by solving the (elastic) seismic wave equations. Forward modeling requires a subsurface model which contains elastic parameters such as the density, compressional (P) and shear-wave (S) velocity and may include attenuation properties. Forward modeling of elastic waves also requires knowledge of the seismic sources. We carried out passive and active seismic noise characterization studies at Terziet in Limburg, the Netherlands, that are aimed at providing estimates for all these parameters.

Passive seismic methods use the ambient seismic noise which can be either natural or anthropogenic in origin to image the subsurface. The behavior and strength of seismic noise depends on several factors, such as the depth of the measurement, atmospheric and weather conditions, geographical location, local geology, tectonic activity and source mechanism. Seismic noise measured on the Earth's surface is dominated by surface waves [14], although recent studies [15] have shown the presence of body waves in short-period seismic noise. An aerial array allows one to form the frequency-wavenumber (f-k) PSD, which is one of the most common

ways of characterizing noise wavefields [16–18]. This is usually accomplished with a beamforming algorithm [19] (described in section 2.3) which essentially decomposes the wavefield in a narrow frequency band into plane waves parameterized by their ray parameter and back-azimuth (i.e. the direction toward the source). With an aerial array of seismometers we can measure the actual propagation velocity of a horizontally traveling wave. Such array studies of microseismic noise in the frequency band 0.05 to 0.3 Hz have been reported by [20–24]. In the high-frequency band, above 2 Hz, where noise sources are mostly anthropogenic in origin [18, 25, 26], have shown useful applications of array-based data analysis methods despite the presence of several non-stationary noise sources and lack of coherence in the ground motion measured by seismometers that are a few wavelengths apart.

In this paper we implement beamforming on several weeks of ambient noise data collected with two surface arrays of seismometers. We compute the surface-wave dispersion, the frequency dependent direction of propagation of surface waves, and also infer the modal composition of the surface-wave noise. The surface-wave dispersion is further used to estimate a shallow subsurface S-wave velocity model [27]. Estimation of subsurface models from the observed surface-wave dispersion requires constraints to be imposed on the velocity-depth search space. For this we made use of the geological and geophysical logging information obtained from a 140 m deep borehole that we drilled at the site in 2017. Standard geophysical investigations using resistivity logging, sonic logging, and gamma-ray logging were employed [28]. These methods help in understanding the composition of each of the subsurface layers and provide estimates of the density, P-wave and S-wave speeds of these layers. The geophysical interpretation of the subsurface layers is discussed in section 3.

Active seismic surveys were conducted to obtain an estimate of the subsurface P-wave velocity model. Active studies were needed as the sensitivity of the observed surface-wave dispersion to changes in subsurface P-wave velocity and density in the passive studies is insufficient [29]. In active seismic applications, a signal of known strength and phase is injected into the subsurface and then recorded by an array of seismometers. The subsurface response comprising direct waves, refracted waves, reflected waves and surface waves are analyzed to image the subsurface. In most cases, the reflected signal travel-times are used to derive the body-wave velocity of the different subsurface layers. However, for our case, due to the presence of guided waves [30], reflected signals could not be delineated and hence we made use of refraction travel-time inversion schemes [31] to obtain a shallow P-wave velocity model of the region.

For an understanding of the subsurface noise composition, concurrent measurements of seismic noise were carried out by two permanent broadband seismometers, one installed on the surface and the other at a depth of 250 m. Additionally, this allowed to estimate the total attenuation for both surface and body waves to this depth.

The workflow of the paper is as follows. Section 2 presents the main characteristics of the surface and underground seismic noise. Results from beamforming on the passive seismic data are used to infer the existence of surface-wave modes in the noise. Three-component noise measurements with broadband surface and underground sensors are used to estimate the Rayleigh-wave ellipticity and the horizontal to vertical spectral ratio (HVSR). In section 3 we derive the P-wave and S-wave velocity models by using the active and the surface array measurements. We also discuss the results from the borehole logging that are used to constrain the velocity models. In section 4 we present an interpretation of the composition of the seismic noise observed on the surface and underground. Finally, the conclusions of this work are presented in section 5.

2. Ambient noise characterization

The assessment of surface seismic noise is important to determine the extent to which the low-frequency sensitivity of a subsurface gravitational-wave telescope will be limited. Array analysis of the noise allows us to decompose the wavefield into its constituent wave modes, and to determine the relative (source) strengths and angles-of-incidence. These strengths and angles for each propagation mode can then be used as input for modeling the surface and underground seismic noise.

The first step in passive data analysis is the design of an array geometry that can sample the spatio-spectral attributes of the seismic noise in a desired frequency band. Low-frequency surface waves propagate with higher velocities due to their higher depth of penetration in the subsurface. Thus, they are characterized by longer wavelengths and hence large-aperture seismic arrays are needed to resolve their arrival times. The opposite is true for high-frequency surface waves, which are sensitive to shallow subsurface velocities and have shorter wavelengths [32]. A study by [33] proposed that the maximum array aperture should be at least greater than the maximum wavelength of interest and the minimum sensor separation must be smaller than half the minimum wavelength of interest. The second condition follows from the Nyquist criterion to avoid spatial aliasing at shorter wavelengths. Moreover, the array must have symmetry in its response to surface waves propagating along any azimuth. In order to satisfy all the above mentioned criteria, the concept of theoretical array response [34] is suitable for designing seismic arrays capable of analyzing surface waves in a given frequency band of interest. Here we analyze surface waves in the frequency band 2.4–14.0 Hz.

2.1. Sensor layout

Two arrays of vertical-component seismometers distributed along the circumference of rings of varying radii were used. Note that similar array geometries have already been used for surface-wave studies at the Advanced Virgo detector site [18, 35]. Figures 2(a) and (b) show the array layout on a map of the region and in Cartesian coordinates, respectively. Array A comprises six rings of seismometers with the radius increasing as $r_0 2^{n-1}$ where $r_0 = 3.5$ m and $n \in \{1, 2, 4, 5, 6, 7\}$. The nth ring has $(2n - 1)$ sensors equally spaced in azimuth; there is one sensor at the center of the array. The minimum and the maximum radius of array A are 3.5 m and 228 m, respectively. Array B is similar to array A, but has five rings of seismometers and hence a maximum radius of 56 m. The circular layout of each of the arrays ensures symmetrical response to surface waves impinging on the array from all directions [36].

Combining arrays A and B, a total of 74 seismometers were deployed at Terziet, Limburg in the Netherlands for a period of 25 days between November 4 and November 28, 2017. Data were acquired at a sampling rate of 250 ms, and a maximum possible preamplifier gain of 24 dB was used to maximize the signal to noise ratio.

2.2. Surface noise characteristics

The PSD of the measured seismic noise was computed with Welch's method [37]. For every seismometer, the data were divided into 10 min segments with a 25% overlap between consecutive time windows, and PSDs were computed for every such window. Figure 3(a) shows the PSDs averaged over all 10 min windows for Friday, November 10, 2017. The data are representative of seismic noise typically observed on weekdays. For clarity we plot the PSDs of only four of the seismometers which are marked in figure 2(b). Peterson's new high-noise and low-noise models (NHNM, NLNM) [38] are plotted for comparing the seismic noise level at Limburg to the global average. Peaks in the PSDs between 0.1 and 0.4 Hz are due to the

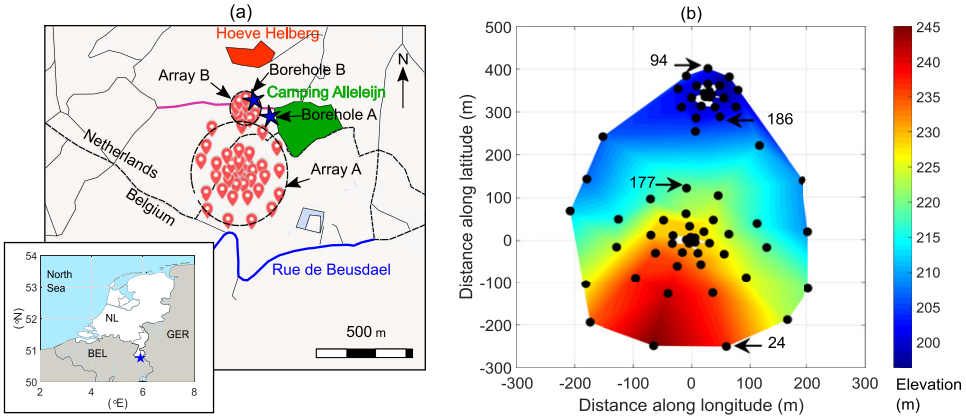

Figure 2. (a) Layout of array A and array B showing seismometers laid out on rings of different radii on a map of Terziet, Limburg. The two boreholes at the site are marked with stars. Map data ©2020 Google. (b) Sensor geometry shown on a Cartesian coordinate system and overlaid on the topography at the site. Black solid dots show four seismometers along with their sensor ID; their noise power spectral densities are shown in figure 3(a).

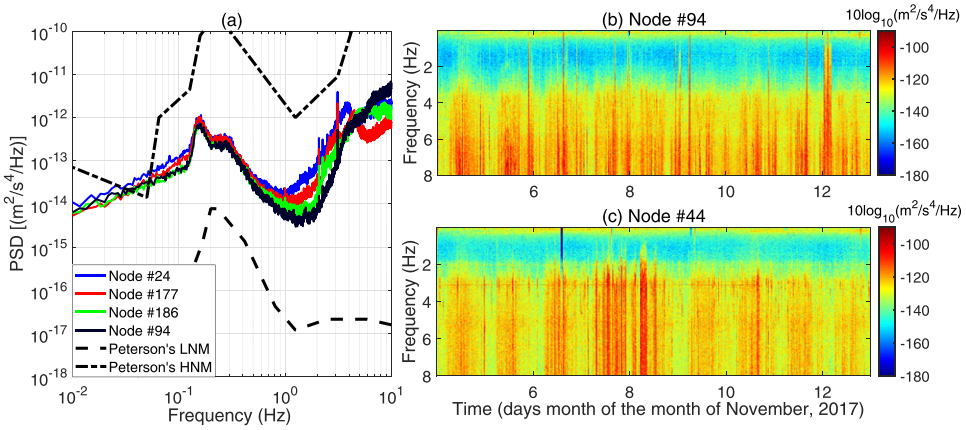

Figure 3. (a) PSD on Nov. 10, 2017 of the four seismometers marked by arrows in figure 2(b) showing microseismic noise at frequencies below 1 Hz and anthropogenic noise above 2 Hz. (b) and (c) Show spectrograms of the seismic noise featuring the diurnal variation for frequencies above 2 Hz.

secondary microseism attributed to the interaction of ocean swells with the shallow seafloor [39]. In the frequency band 0.5 to 2 Hz the origin of seismic sources shifts from natural to anthropogenic. Figures 3(b) and (c) show the variation in PSD of the measured seismic ground-acceleration as a function of frequency and time. It is evident from the diurnal variation in PSD that the seismic noise above 2 Hz is due to human activities like farming near the site. Noise at night is reduced by an order of magnitude compared to that measured during the day.

2.3. Beamforming

Beamforming is a passive seismic data processing method whereby the coherent part of the ambient seismic noise is decomposed into a set of plane waves defined by their direction of propagation ϕ and slowness p (i.e. the inverse of the wave speed). The signals at different sensors are delayed and stacked. The objective is to estimate the stacked power corresponding to different values of ϕ and p. We have implemented beamforming on concurrent segments of data recorded by all seismometers in the array. A frequency-domain data covariance matrix $R_{xx}(f)$ corresponding to a frequency bin of interest is constructed by dividing the data into N segments. At a desired frequency f and for a seismic array with M seismometers, the data covariance matrix is simply $R_{xx}(f) = X(f)X^*(f)$ where $X(f)$ is an $M \times N$ matrix with each element $X_{ij}(f)$ corresponding to the complex Fourier spectra of the data for the ith seismometer and jth time segment and '*' represents the complex conjugate operator. Secondly, phase delays are applied to the data covariance matrix by using the steering vector $w_k(f)$. The steering vector w_k is an $M \times 1$ column vector expressed as $w_k(f) = [\mathrm{e}^{-\mathrm{i}2\pi f\tau_0}, \mathrm{e}^{-\mathrm{i}2\pi f\tau_1}, \ldots, \mathrm{e}^{-\mathrm{i}2\pi f\tau_{M-1}}]$ where i represents the complex variable and $\tau_m = x_m p_k \cos\phi_k + y_m p_k \sin\phi_k$ is the time delay for a plane wave propagating with slowness p_k and along an azimuth ϕ_k to reach the seismometer located at coordinates (x_m, y_m). Since delays are applied to the data covariance matrix as a function of azimuth and slowness of the propagating plane wave, the beampower $B(f)$ is a function of slowness and azimuth at a desired frequency f and can be expressed as

$$B(p_k, \phi_k, f) = \frac{1}{N} w_k R_{xx} w_k^*. \tag{2.1}$$

The value of beampower B given in equation (2.1) is computed for several combinations of (p, ϕ) and the combination that yields the maximum beampower gives an estimate of the dominant direction and slowness of plane-wave propagation at that frequency.

Beamforming was implemented on every concurrent one-hour record of seismic data from all seismometers after correcting the data for instrument irregularities and glitches. The beampower was computed corresponding to 180 values of azimuth ranging between 0 and 358° at an interval of two degrees and for all slowness values between 4×10^{-4} and 10^{-2} s m^{-1} at an interval of 2.5×10^{-5} s m^{-1}. Hence, a total of 69 300 steering vectors were used. The computed beampowers are then averaged over all hours of the measurement period. Figure 4 shows the beampower distribution as a function of slowness and azimuth at six discrete frequencies for passive seismic noise data acquired by array A. The distribution at each frequency appears as a ring in a particular slowness interval with the dominant peak between azimuths of 180° and 225°. This direction corresponds to noise originating from the road 'Rue de Beusdael' running south of the array. In addition, noise propagating from north-east was observed at 5 Hz and higher. This noise was due to farming activities at the adjacent camping ground. Below frequencies of 5 Hz, the fundamental mode of Rayleigh waves dominates the vertical component of seismic noise. However, at frequencies greater than 5 Hz, higher-order modes of Rayleigh waves are observed besides the fundamental mode. These higher-order modes can be visualized as a superposition of reflected P-waves and vertically polarized S-waves (SV) and hence propagating with higher apparent velocities. Consequently, for a given frequency, higher-order modes are sensitive to the velocities of deeper subsurface layers as compared to the fundamental mode. Observation of higher-order Rayleigh-wave modes in surface seismic noise is a common phenomenon in geologies where a sharp contrast in velocities exists between layers at shallow depths [40]. Additionally the source mechanism generating the noise plays a role in the modal content of the observed surface noise.

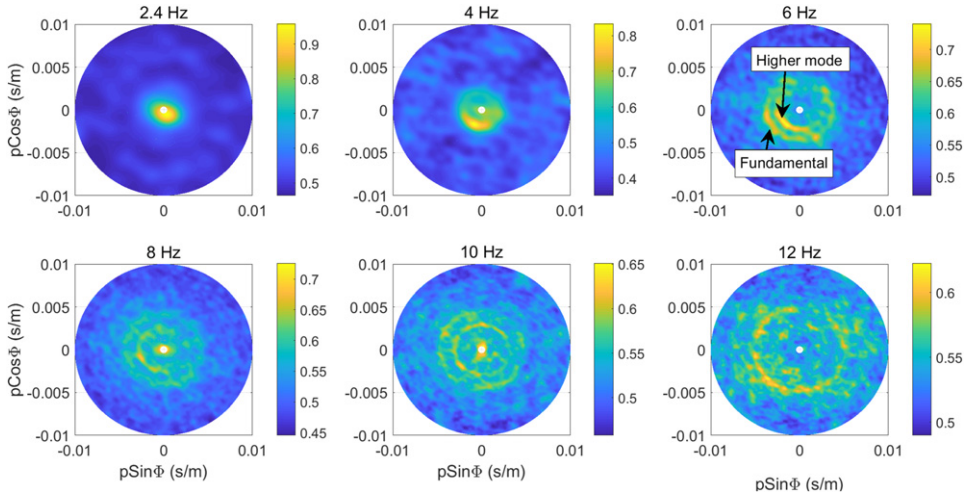

Figure 4. Beamforming results for ambient noise data (vertical component) acquired by array A between Nov. 4 to 28, 2017 at frequencies of 2.44, 6, 8, 10, and 12 Hz. The radial axis shows slowness (4×10^{-4}–10^{-2} s m^{-1}), and the azimuth is measured clockwise from North. Low-frequency noise below 5 Hz propagates as the fundamental mode of Rayleigh waves originating mostly south of the array. At frequencies greater than 5 Hz the noise source distribution is more isotropic, and the first overtone of Rayleigh waves is observed besides the fundamental mode.

Beamforming was also implemented on the seismic noise data acquired by array B. The smaller array aperture of about 112 m limited beamforming to frequencies above 3 Hz. Figure 5 shows the beamforming results at six discrete frequencies. Seismic noise in the frequency band 3 to 3.4 Hz is dominated by surface waves propagating from the road 'Rue De Beusdael'. For frequencies between 3.8 and 5.4 Hz noise sources originating north from farming activities at a nearby camping ground 'Hoeve Helberg' dominate the measured noise spectrum. For frequencies greater than 5.8 Hz, an isotropic distribution of noise sources is observed with some bias toward the source in the north and the camping ground located east of array B. A dominant first overtone is observed for frequencies greater than 10 Hz. Between 8 and 10 Hz, propagation velocities of the first overtone increases drastically and the limited array aperture prevents accurate identification of the phase velocities.

The beamforming results shown in figures 4 and 5 are used to estimate the slowness of the surface waves at a particular frequency. This is accomplished by summing up the beampower across all azimuths. The beampower is now expressed only as a function of slowness and the peaks in beampower provide an estimate of the slowness of the different modes of surface waves. On repeating this process for different frequencies, we can construct the 'surface-wave dispersion curve' which is shown in figure 6.

Rayleigh-wave phase velocities are estimated by using the beamforming output from array A and array B in the frequency bands 2.4 to 14.0 Hz and 3.0 to 14.0 Hz, respectively. Figure 6(a) shows the beampower distribution as a function of frequency and velocity. The fundamental Rayleigh-wave mode contributes dominantly up to 5 Hz. Between 5 and 8 Hz, the first overtone and the fundamental mode contribute about equally. An alternate branch of the first overtone is observed at 8 Hz and is shown with the black-dashed curve. This can be due to in-homogeneity of the medium. The magenta curve indicates the presence of the second Rayleigh-wave overtone. However, it suffers from weak SNR and hence is not well resolved.

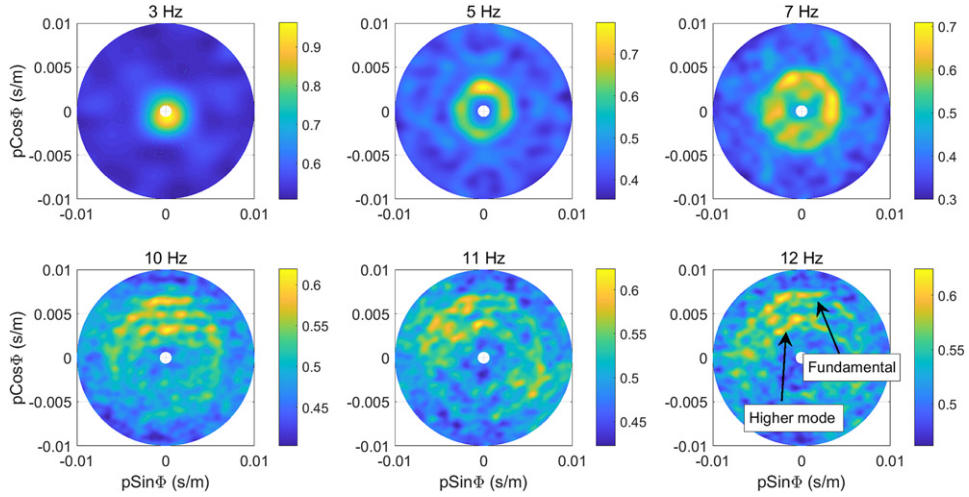

Figure 5. Beamforming results for ambient noise data (vertical component) acquired with array B between Nov. 4 to 28, 2017 at frequencies of $3, 5, 7, 10, 11$ and 12 Hz. The radial axis represents slowness (6.67×10^{-4}–10^{-2} s m^{-1}) and azimuth is measured clockwise from North. A shift in the noise propagation direction is observed from South to North as we move from 3 Hz to higher frequencies. Beyond 7 Hz the direction of noise propagation is more isotropic.

Figure 6(b) shows the phase-velocity estimates obtained with array B. For frequencies greater than 8 Hz, Rayleigh waves propagate both as fundamental mode and as first overtone. Observation of the first Rayleigh-wave overtone at high frequencies is representative for a soft-soil to hard-rock transition at shallow depths. Figure 6(c) shows a comparison of the phase velocities derived from beamforming of array A and B data. Fundamental-mode phase velocities for both arrays are similar for frequencies below 7 Hz. Array B shows a sharp drop in phase velocities between 3 and 3.5 Hz and between 7 and 8 Hz unlike array A where the velocities drop sharply between 4 and 5 Hz and decreases smoothly thereon. These sharp changes in phase velocity correspond to the transition from one subsurface layer to an other. The difference in these transition-frequencies implies that the transition-depth of the subsurface layers varies between array A and B. Also for frequencies greater than 8 Hz, the velocities obtained for array A are higher than those observed for array B. Overall, the two dispersion curves point to a significant lateral inhomogeneity in the subsurface geology. A more detailed description of the subsurface model at Terziet is given in section 3.

2.4. Underground noise characterization

We characterize the underground seismic environment with a Streckeisen STS-5A seismometer [41] stationed at a depth of 250 m inside a 260 m deep borehole which is shown as borehole B in figure 2(a). In addition, a Nanometrics Trillium-240 seismometer is positioned on the surface of borehole B. Ambient noise data used in the analysis were acquired simultaneously by both seismometers in the period Nov. 2019 to Oct. 2020.

PSDs of the seismic noise are obtained for the entire recording period with 10 min segments. Figure 7 shows the PSD of the surface and the underground seismometer. Both the horizontal and vertical components of the seismic noise are shown. For frequencies between 0.1 and 0.5 Hz, PSDs measured on the surface and underground are identical. This is because the depth

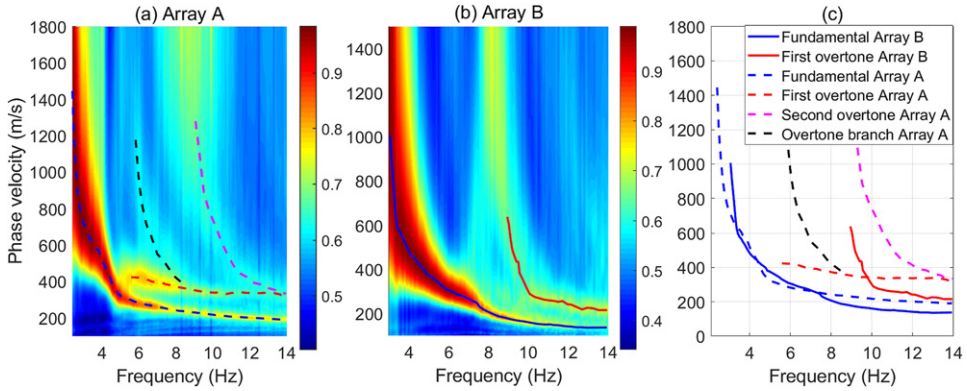

Figure 6. (a) Rayleigh-wave phase velocity estimated with beamforming of data measured by array A. The blue-dashed curve shows the fundamental-mode phase velocity for Rayleigh waves and the red-dashed curve shows the first overtone which is observed only at frequencies greater than 5.4 Hz. Possible other higher-order modes are indicated by the dashed black and magenta curves. (b) Rayleigh-wave phase velocity for array B. The blue- and the red-solid curves show the fundamental and first overtone of the Rayleigh wave. (c) Comparison of the phase velocities derived from array A and B data for the observed Rayleigh-wave modes.

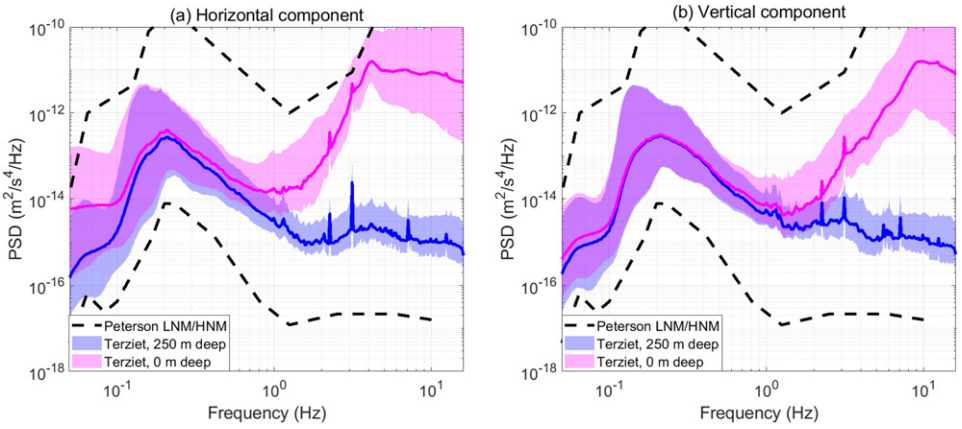

Figure 7. (a) The magenta and the blue curves show the mean PSD of the horizontal component of seismic noise measured between Nov. 2019 and Oct. 2020 on the surface and underground, respectively. The shaded regions correspond to the 10th and the 90th percentiles of the measurements. (b) Same as (a) but for the vertical component of the seismic noise. Peterson's low noise model (LNM) and high noise model (HNM) are plotted for comparison with global observations.

at which the underground measurements are carried out is only a fraction of the wavelength of the waves in the microseismic frequency band and the noise propagates unattenuated.

The surface PSDs show moderate levels of anthropogenic noise at frequencies above about 2 Hz (see also figure 9). This noise is most likely due to local traffic and farming activities. The subsurface PSDs show that the surface noise quickly attenuates with depth. Surface-wave attenuation is a function of frequency and depends strongly on the subsurface velocity profile.

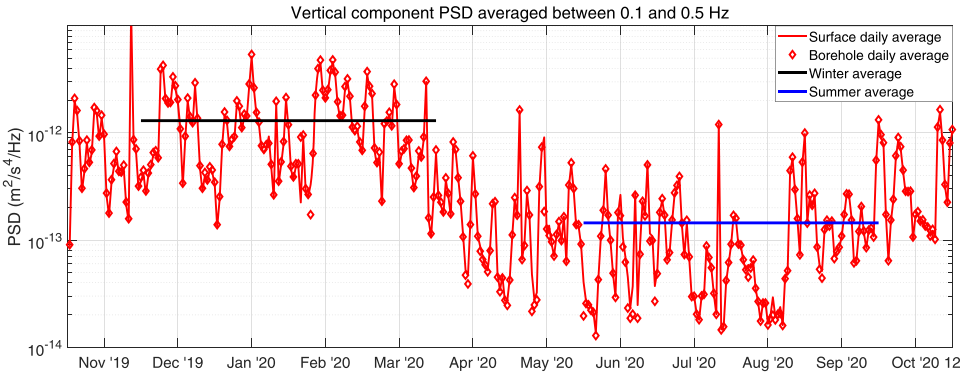

Figure 8. Temporal variation of the vertical component of the seismic noise PSD averaged in the frequency band 0.1 to 0.5 Hz. The red dots and dashed curve represent the surface and underground measurements, respectively. The horizontal black and blue lines represent the average PSD during winter and summer months, respectively.

This is further discussed in section 4.1. In addition, at high frequencies anelastic processes may cause significant attenuation, especially in unconsolidated (saturated) soils such as those found at the surface in Terziet. Hence, figure 7 hints at a geology favorable for attenuating surface noise.

Surface waves in the microseismic frequency band originate due to the interaction of ocean waves with the continental landmass. Hence, an increased wave height in the sea during a storm can lead to an increase in microseismic noise [42]. For example [43], studied seismic noise measurements from a global network of seismometers and concluded that the power of microseismic noise is generally observed to be higher during winter than in summer. It is indirectly related to the seasonal variability and the fact that storms in the ocean occur more often in winter than in summer. To test whether this seasonal variability was visible in our measurements, the vertical component PSD averaged in the band 0.1 to 0.5 Hz is shown as a function of time in figure 8. The microseismic noise reduces by an order of magnitude during the summer compared to winter months.

For frequencies greater than about 2 Hz, surface seismic noise is attenuated when going underground and mostly it is anthropogenic in origin. This so-called cultural noise is typically due to cars driving on nearby roads and bridges, and industrial and farming activities in the vicinity of the site. This was also observed from the surface array measurements discussed in section 2.2. Due to its anthropogenic origin, the noise power in this frequency band has a typical diurnal variation. Figure 9(a) shows the temporal variation of the surface and underground seismic noise averaged in the frequency band 2 to 10 Hz. The noise measured on the surface shows a strong day and night variation, with the seismic noise PSD during the night showing a reduction of over two orders of magnitude compared to that during the day. On the contrary the underground noise measurements during night show only a reduction in seismic noise PSD by a factor 3 to 4 compared to that during the day. Figure 9(b) shows the diurnal variation and a further reduction in underground seismic noise during weekends.

2.5. Horizontal to vertical spectral ratio and Rayleigh-wave ellipticity

The peak amplitude and frequency of the HVSR of seismic noise can be used to characterize the shallow geology at the site and its attenuation properties. A large HVSR is observed due to the sharp impedance contrast at shallow depths. The frequency of the HVSR peak can also

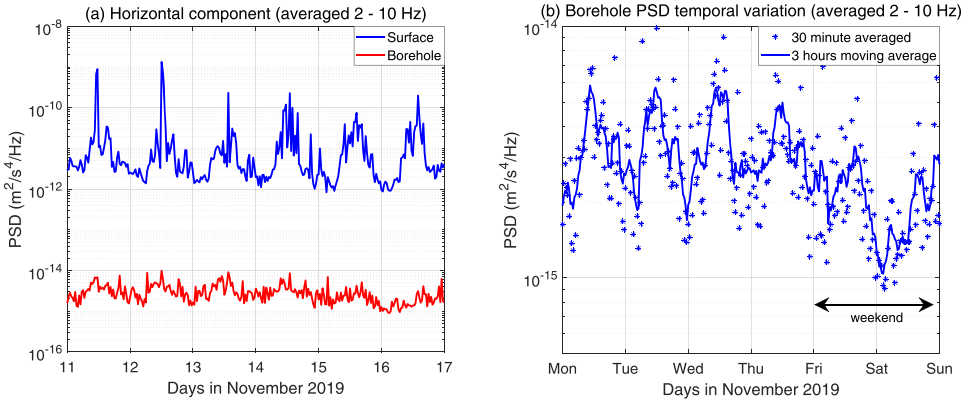

Figure 9. (a) Temporal variation of the horizontal component of the ambient seismic noise PSD averaged in the frequency band 2 to 10 Hz for November 11 to 17, 2019. The red and blue curves represent the surface and underground measurements, respectively. Strong diurnal variation is observed for the surface noise. (b) Diurnal variation by only a factor of 3 to 4 is observed for the underground seismic noise. A further reduction by a factor 2 is observed during weekends when compared to that during weekdays.

be used to determine the depth to hard-rock, given that the shear-wave velocity of the soft-soil is known [46]. Additionally, the estimated Rayleigh-wave ellipticity along with HVSR measurements can be used to determine the contribution of different Rayleigh-wave modes to the total seismic wavefield. The vertical component noise peaks at about 9 Hz and shows a flat trend for greater frequencies. On the contrary the horizontal component peaks at about 4 Hz. This difference between horizontal and vertical component implies a large HVSR which peaks at about 4 Hz. The magenta curves in figures 10(a) and (b) show the HVSR corresponding to the surface and underground noise measurements for the 10 days measuring period from Nov. 1 to 10, 2020. Estimation of the HVSR was done using the guidelines under the SESAME [45] recommendations (i.e. only far-field ambient noise was used and transients were removed). Since it is the stationary part of the seismic noise that is used for the estimation, the peak frequency of HVSR gives us the fundamental resonance frequency at the site. A large HVSR of about 8 is observed which implies a strong impedance contrast in the subsurface at a shallow depth. For a simple soft-soil over half-space model, we can use the fundamental frequency f_0 of the site to estimate the depth to bedrock given the soft-soil S-wave velocity $V_{\mathrm{S/Surf}}$, or vice versa [46]. The minimum depth to bedrock h_{min} is approximated as $V_{\mathrm{S/Surf}}/4f_0$. In our case an average S-wave velocity between 200 and 300 m s^{-1} yields a minimum depth to bedrock of about 15 to 20 m. The HVSR estimated at 250 m depth shows a peak magnitude of about 2 at 4.5 Hz. This is because the borehole-seismometer is already positioned on hard rock and measures little noise amplification unlike the case on the surface.

The vertical component of the seismic noise is composed of P-waves, vertically polarized S-waves (SV) and the vertical component of the Rayleigh waves. Horizontally polarized S-waves (SH), Love waves and the radial component of the Rayleigh waves constitute the horizontal seismic noise field. Therefore a large HVSR could be due to the dominant presence of SH waves at the site or even Love waves. From HVSR estimations alone it is impossible to determine the composition of the noise wavefield, as it is a mixture of Rayleigh, Love and body waves. Hence, we compute the Rayleigh-wave ellipticity at the site by using the random-decrement method which has been discussed in [47]. The blue curves in figures 10(a) and (b) show the

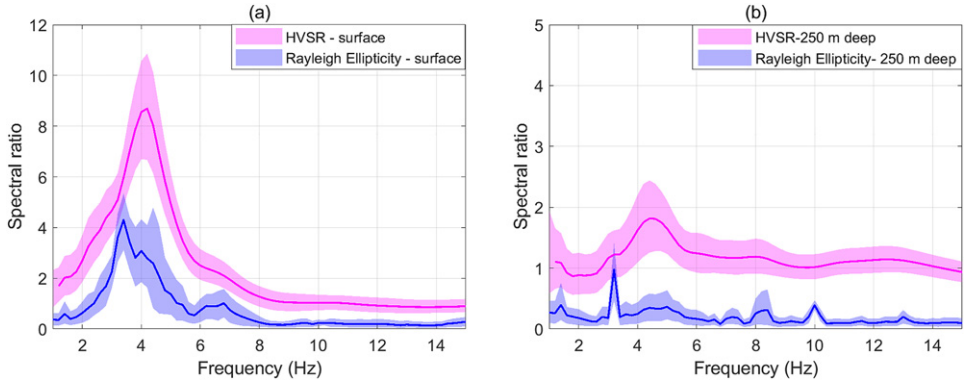

Figure 10. (a) Estimated surface HVSR and Rayleigh-wave ellipticity. The magenta- and blue-shaded regions show the 10th and the 90th percentiles. (b) Same as (a), but corresponding to the measurements at 250 m depth.

estimated Rayleigh-wave ellipticity as a function of frequency for the surface and 250 m deep measurements, respectively. The surface Rayleigh-wave ellipticity peaks at 3.2 Hz followed by another small peak at about 7 Hz. Comparing the HVSR and the Rayleigh-ellipticity curves on the surface we can infer that the major contribution of the radial component of Rayleigh waves on the horizontal seismic field is in the frequency band 1–3 Hz and 5–7.5 Hz. The second peak in the Rayleigh-wave ellipticity at about 7.2 Hz could be due to the ellipticity peak of the first overtone of the Rayleigh wave. These peaks at 3.2 and 7.2 Hz also coincide with the peaks that are observed in the surface and the underground noise spectra shown in figures 7(a) and (b). In addition to these peaks, several other peaks at 8.4, 10, 11.6 and 13 Hz are observed in the underground Rayleigh-wave ellipticity curve. These peaks could be due to the ellipticity peaks of higher-order modes of Rayleigh waves, which are more sensitive to deeper subsurface structures than the fundamental mode. Hence, these spectral peaks are not observed strongly in the surface-noise spectrum. Moreover, these peaks are stationary in magnitude and peak-frequency, and can be interpreted as the poles of the higher-order modes of the Rayleigh-wave eigenfunctions. However, before any definitive conclusions on the nature of these peaks can be drawn, additional measurements should be carried out in search of possible external sources (e.g. machinery, windmills).

2.6. Regional earthquakes

The borehole site is situated about 15 km west of Aachen, which is located in a complex geologic and tectonic position at the northern margin of the Variscan deformation front at the borders between the Brabant Massif, the Hohes Venn/Eifel areas and the presently active rift zone of the Lower Rhine Embayment [48]. The site is located about 80 km west of Cologne which is also a part of the Lower-Rhine-Embayment and displays basin-like subsidence and hence has been a source of several earthquakes [49].

In this study we use the data recorded by the borehole seismometer in the period Jan. 1, 2020 to Jan. 31, 2021 in order to understand the influence of regional earthquakes on the performance of Einstein Telescope at the Terziet site. A total of 142 earthquakes were observed by KNMI during this period and the locations are shown by the solid dots in figure 11(a). Most of these earthquakes originate either in the Aachen–Cologne region or in the natural gas fields in Groningen [50]. From these Groningen earthquakes only those with moment magnitude

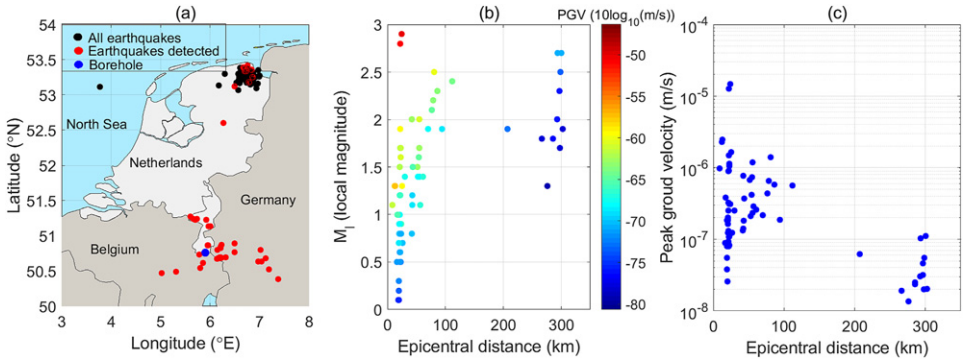

Figure 11. (a) A map of Netherlands-Belgium-Germany showing the location of the earthquakes (solid dots) near the borehole site. The red (black) solid dots show the location of the earthquakes that were (not) detected at the site. The site at Terziet is shown by the blue solid dot. (b) PGV measured at the borehole site as function of the epicentral distance and the magnitude of the earthquakes. PGV is represented by the colorbar. (c) PGV expressed only as a function of epicentral distance. Nine of all the 71 measured earthquakes may unlock an interferometer.

greater than 1.8 are recorded at the borehole. These earthquakes originate about 300 km away from the site and have a shallow depth of origin of about 3 km. All the earthquakes originating in the Aachen–Cologne–Liège belt were detected. These earthquakes range in magnitude from 0.1 to a maximum of 2.9 and originate at depths between 5 and 18 km. The red solid dots in figure 11(a) show the location of the earthquakes that are recorded at the site. Of the 142 earthquakes that occurred during the measurement period, 71 were detected at the borehole site. In order to measure the performance of the detector and possible lock-loss during these earthquakes, we use the peak ground velocity (PGV) induced by the earthquake at the borehole for frequencies greater than 1 Hz. Figure 11(b) show the PGV as a function of the epicentral distance and the magnitude. Assuming that the interferometer is expected to lose lock for ground velocities greater than 10^{-6} m s^{-1} [51] we observe that nine of these earthquakes would result in possible interruptions of observation time (caused by losses of detector control). The weakest earthquake that could unlock the interferometer was observed to be of magnitude 1.3 and originated from about 25 km from the borehole and at a depth of 18 km. The maximum ground velocity was induced by a 2.9 magnitude earthquake originating at a depth of 7 km and about 24 km away from the site.

While most of these regional earthquakes would unlock an interferometer a few times in a year, teleseismic earthquakes of magnitudes greater than 4.5 could also result in an interferometer unlock. A total of 243 earthquakes ranging in magnitude between 5 and 7 had a PGV that may unlock an interferometer. Combining both the regional and the worldwide earthquakes and assuming that an interferometer takes about one hour to resume observation, a data loss of about 3% is expected. This is consistent with current experience at the LIGO and Virgo interferometer sites [52].

3. Subsurface model estimation

The Rayleigh-wave phase velocity derived in section 2.3 can be used to derive the subsurface model parameters. It is most sensitive to the subsurface S-wave velocity and least sensitive to the density model [32]. The mapping between a dispersion curve and a subsurface model is not unique, as two different subsurface models can yield the same dispersion curve [53]. Hence

in order to obtain realistic subsurface models from the observed Rayleigh-wave dispersion, several constraints must be set on the parameter space. For this reason, *a priori* information on the subsurface is necessary. We obtained this information from borehole logging at the site.

3.1. Borehole logging

The site at Terziet hosts two boreholes, one with a depth of 140 m (labeled Borehole A) and another of 260 m (Borehole B). Figure 2(a) shows the location of the two boreholes. No logging was performed for Borehole B which hosts the underground seismometer. However, we carried out logging at Borehole A, which is located approximately 100 m east of the center of array B. The drilling and the interpretation of the borehole logs was accomplished in collaboration with industrial partners such as Shell, Deltares and TNO. Gamma-ray, resistivity and sonic logging tools were used. Gamma-ray logging [54] provides information about the clay content of the soil. While a high gamma-ray level indicates the presence of clay-rich soil, a lower gamma-ray value points to clean or coarse-grained sandstone and carbonates. Additionally, spectral gamma-ray logging [55] was carried out to collect information about the content of the naturally occurring radioactive elements potassium (K), uranium (U) and thorium (Th) in the soil. Resistivity logging [56] was performed in the borehole and gives an indication of the porosity of the soil sample. Higher porosity of the material indicates higher conductivity of water, and lower resistivity values. Sonic logging gives an estimate of the P-wave velocity of the subsurface and is based on measuring the travel-time of waves propagating between a transmitter and a receiver in the borehole.

Figure 12 shows the different borehole log curves. The top 3 to 4 m of the subsurface consists of clay. Changes in Th and K gamma-ray levels between 5 and 12 m indicates a change to a layer with reduced clay content. This layer is also characterized by a low P-wave velocity. The main material of this layer is sandstone. A transition from sandstones to siltstones is observed at about 12 m depth and reveals itself by an increase in the K and Th contribution; see figure 12. However, the resistivity value of this layer is low which indicates the presence of rough gravel. Hence, this layer is a coarse-grained rock conglomerate consisting of sandstone and siltstone. A sharp jump in the P-wave velocity is also observed. Between 35 and 40 m, a clear change in the gamma-ray levels is observed, followed by an increase in resistivity. These changes mark the transition to a different geological formation. This layer mainly consists of micaceous sandstones and shales and is often referred to as the Evieux formation [57]. This alternation between shales and sandstones is clearly visibly in the troughs and peaks observed in the resistivity logs. A drastic increase in resistivity is observed at depths greater than 90 m which indicates the presence of another tight rock formation. The reduction of the gamma-ray spectrum indicates the presence of shale. This formation is also characterized by a further increase in P-wave velocity to about 5.5 km s^{-1}.

3.2. S-wave velocity model estimation

A subsurface velocity model based on the borehole logging and the Rayleigh-wave phase velocity measurements is derived with the stochastic direct search method that makes use of the neighborhood algorithm [58]. It explores the parameter space and finds the subsurface model with the least misfit between the observed and theoretical dispersion curve. Additionally, we use the Rayleigh-wave ellipticity measured on the surface to constrain the estimation of the subsurface model parameters. The misfit for our problem can be expressed as

$$\text{misfit} = \sqrt{\frac{1}{N}\sum_{n=1}^{N}\left(\frac{p^{\text{i}}_{\text{obs}} - p^{\text{i}}_{\text{th}}}{p^{\text{i}}_{\text{obs}}}\right)^2} + \sqrt{\frac{1}{N}\sum_{n=1}^{N}\left(\frac{r^{\text{i}}_{\text{obs}} - r^{\text{i}}_{\text{th}}}{r^{\text{i}}_{\text{obs}}}\right)^2}, \tag{3.1}$$

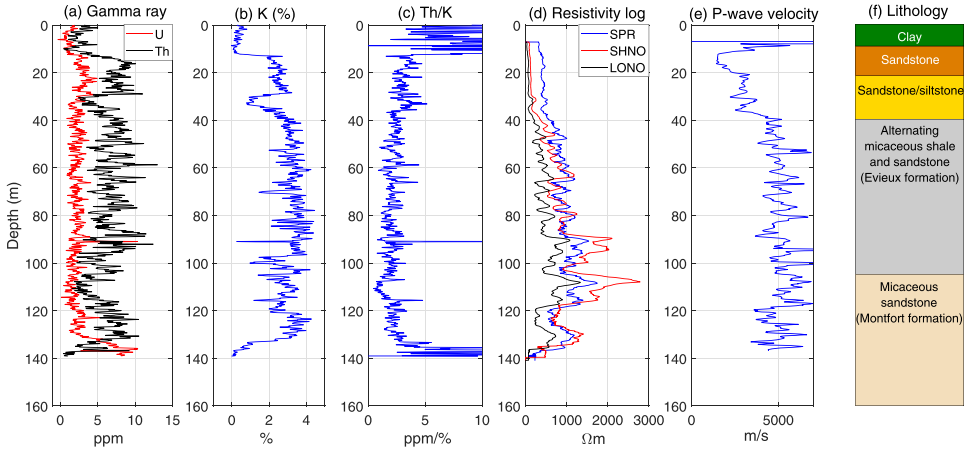

Figure 12. (a) Gamma-ray log to a depth of 140 m showing the uranium (U) and thorium (Th) concentration of the subsurface in units of ppm. (b) Potassium (K) content in the subsurface. (c) Th/K levels in the subsurface in units of ppm/%; a drop in the ratio implies a major formation change. (d) Resistivity log showing the measured single point resistivity (SPR) and the short- (SHNO) and the long-normal (LONO) results. (e) Borehole compensated (BHC) sonic log showing the P-wave velocity of the subsurface. (f) A pictorial representation of the horizontally stratified subsurface geology based on the borehole measurements at Terziet.

Table 1. Parameter search space used for obtaining a 1D subsurface model.

Layer	V_P (km s^{-1})	V_S (km s^{-1})	Depth (m)	Density (10^3 kg m^{-3})	Formation
1	0.2–3.0	0.1–0.5	2–12	1.6–1.7	Clay/Vaals
2	0.2–2.0	0.1–0.7	12–25	1.7–2.0	Sandstone
3	1.0–5.0	0.15–1.2	25–50	1.7–2.0	Sandstone/siltstone
4	3.0–5.0	0.7–2.0	80–140	2.0–2.4	Evieux
5	3.0–6.0	0.7–2.0	200–240	2.2–2.6	Monfort
6	3.0–6.0	1.0–3.0	300–350	2.2–2.8	Esneux
7	4.0–6.0	1.5–4.5	∞	2.4–3.0	Half-space

where p_{obs} and pth represent the observed and theoretical phase velocities, r_{obs} and rth the observed and theoretical Rayleigh-wave ellipticity on the surface and N the number of frequency samples over which the misfit is computed. Applications of this scheme for obtaining reliable shallow S-wave models have been reported previously in [27, 59, 60].

An important objective for carrying out the inversion is to estimate the depth at which the soft-soil to hard-rock transition occurs. A geology with soft soil over hard rock is ideal for attenuating the surface seismic noise at depth. As the shallow geology at Limburg comprises several complex fault systems and the depth to hard rock varies between 15 and 40 m, we perform the dispersion curve inversion separately for array A and B. The Rayleigh-wave ellipticity was used for constraining the subsurface model for array B. For array A, the inversion is unconstrained with respect to the Rayleigh-wave ellipticity. Hence, the subsurface model estimated for array A may not reproduce the correct Rayleigh-wave ellipticity when used in simulations. Table 1 states the search range that was used for estimating the subsurface parameters.

The derived subsurface models corresponding to array A are shown in figures 13(a)–(c). The colorbar shows the misfit of each of the dispersion curves. The explored dispersion curves

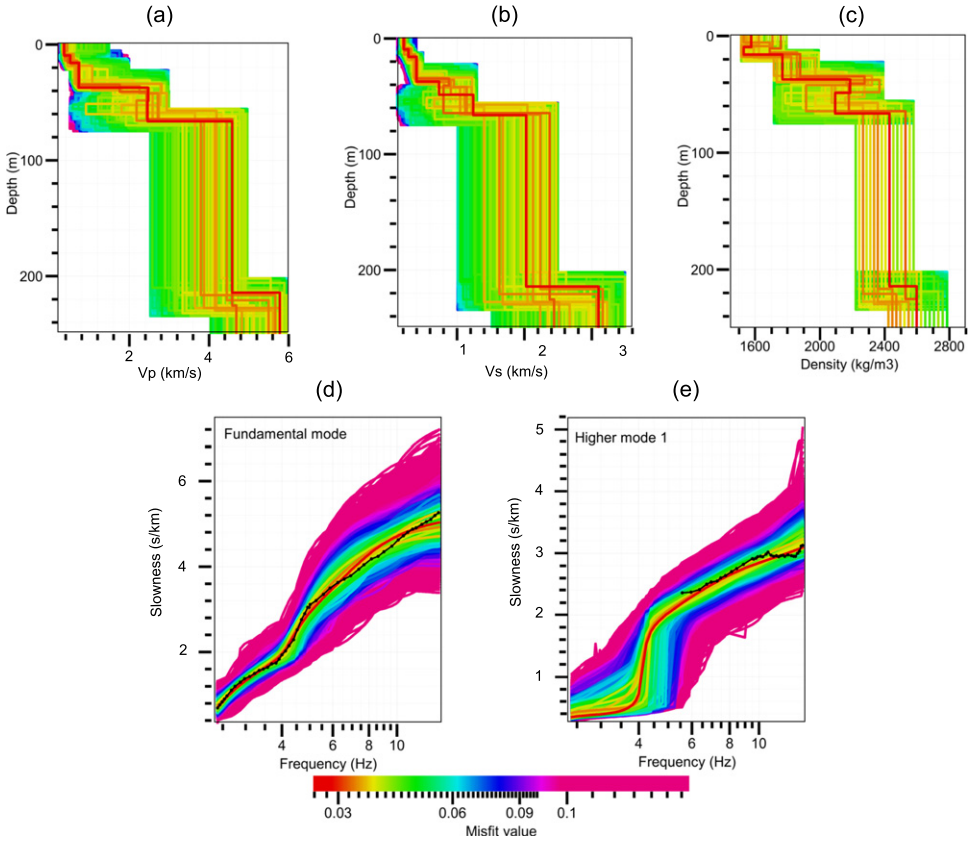

Figure 13. Explored (a) P-wave, (b) S-wave and (c) density models of the subsurface corresponding to array A. (d) and (e) Show the fundamental mode and first overtone of the Rayleigh-wave dispersion corresponding to the subsurface models shown in (a)–(c). The misfit with the observed dispersion curve is represented with the colorbar and the black curves in (d) and (e) represent the observed dispersion curves.

corresponding to the fundamental and the first overtone of Rayleigh wave dispersion are shown in figures 13(d) and (e), respectively. Figures 14(a)–(c) show the results obtained for array B. Here, the subsurface model estimation is further constrained by using the observed Rayleigh-wave ellipticity on the surface. Figures 14(d) and (e) show the different dispersion curves explored during the subsurface model estimation corresponding to the fundamental mode and the first overtone of Rayleigh-wave propagation, respectively. The corresponding Rayleigh-wave ellipticity curves explored while estimating the subsurface model are shown in figure 14(f). The black curves represent the observations and the misfit is represented with the colorbar.

The velocity models for the subsurface for array A and B provide information about the depth at which the transition from soft soil to hard rock occurs. The top soil at the site is clay, mainly deposited due to Saalian and Wurmian glaciation during the Pleistocene period [61]. The layer extends to depths of about 4 m, and is followed by the Vaals formation, which is characterized by a sharp drop in P-wave velocities. It was formed during the late Cretaceous period and comprises loamy sand called glauconite. It extends to depths of approximately 10 to 15 m. A layer of sandstone and siltstone conglomerate is found between 15 and 30 m.

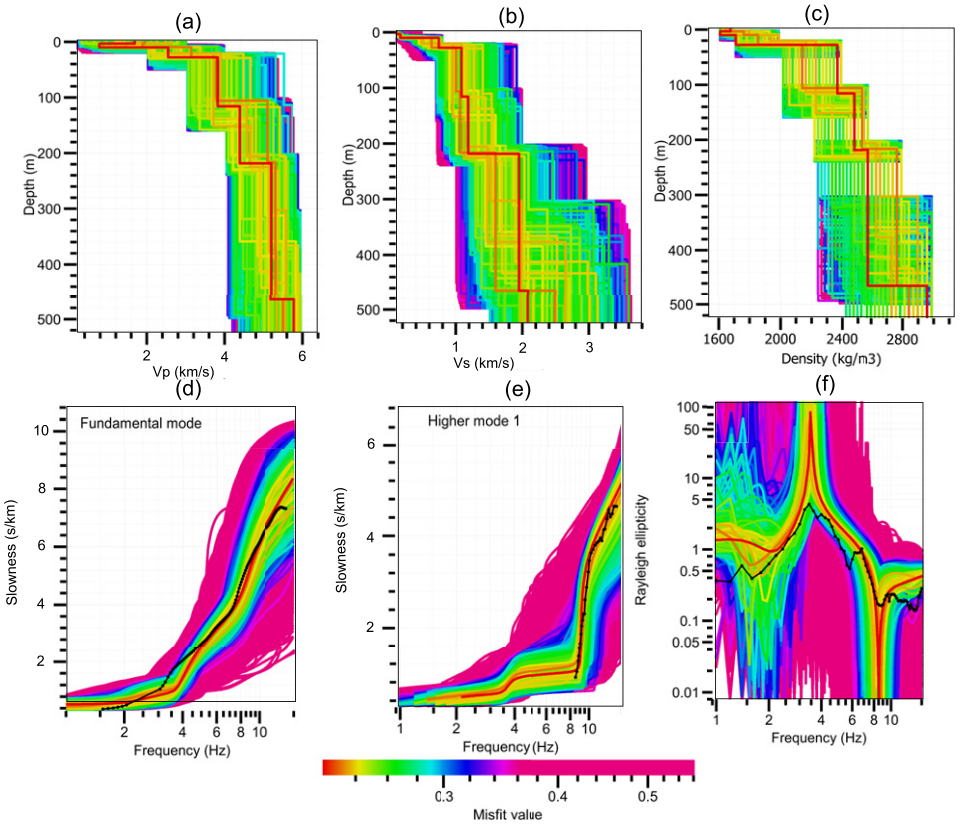

Figure 14. Explored (a) P-wave, (b) S-wave and (c) density models of the subsurface corresponding to array B. (d)–(f) Respectively show the fundamental mode and first overtone of the Rayleigh-wave dispersion and ellipticity corresponding to the subsurface models shown in (a)–(c). The misfit with the observed dispersion curve is represented with the colorbar and the black curves in (d)–(f) represent the observed quantities.

The transition to higher subsurface P and S-wave velocities is already observed between 15 and 20 m. Beyond this the transition to higher P-wave velocities between 3 and 4 km s^{-1} is observed. The starting of the next layer is observed between 100 and 120 m. This transition is at a lower depth for array A as compared to array B. This difference can be explained due to overthrust faulting at the site. This feature is also addressed in section 3.3.3 where we estimate a 2D P-wave velocity model by applying refraction tomography on active seismic data.

3.3. P-wave velocity model estiation

Unlike passive seismic data analysis where surface waves are used to image the subsurface, active seismic methods use the body-wave response of the medium to derive subsurface velocity models. The subsurface is excited by a signal of known amplitude and phase and the response of the subsurface is then measured by an array of seismometers. The response of the subsurface to the injected source signal is composed of body waves, guided waves [30] and surface waves. Body waves include direct waves traveling between the source and receiver, refracted waves from shallow subsurface layers and reflected waves. Reflected waves also include the case when the down-going wave encounters multiple reflections within the same layer. Typically, the travel-time of these reflected waves are used to compute the subsurface P-

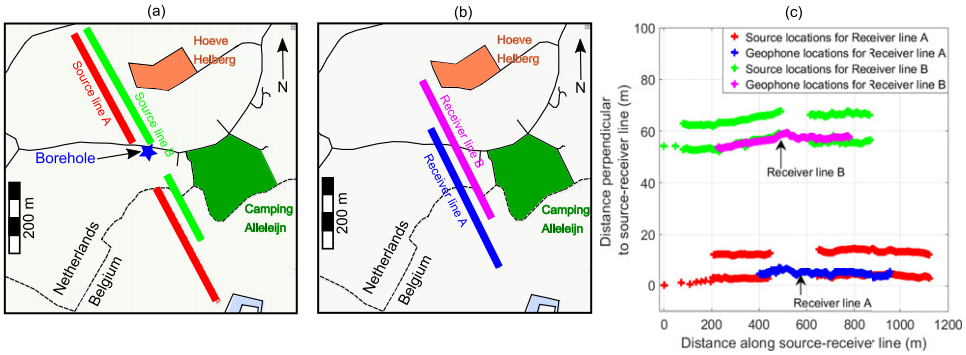

Figure 15. (a) Seismic shot lines shown on a map of the region. Each of the red and green lines corresponds to a particular receiver line. Map data ©2020 Google. (b) Receiver lines A (blue) and B (magenta) are separated by a distance of about 50 m. (c) Shot and receiver line layout shown in Cartesian coordinates.

wave velocities. In cases where these reflected phases cannot be delineated, the direct and the refracted-wave travel-times can be used to infer a shallow subsurface P-wave velocity model. Unlike reflection-data analysis which provides us with deep subsurface information, refraction processing can provide an image down to a depth of about 25% of the maximum source-receiver separation [62].

3.3.1. Source-receiver layout. Active seismic data were acquired with two receiver lines from Feb. 19 to Mar. 01, 2018. Figures 15(a) and (b) show the shot and receiver line spread on a map of the region. A shot is referred to as the seismic signal injected into the subsurface by using an explosion or other mechanical methods (described in section 3.3.2). Receiver lines A and B had 182 and 179 seismometers, respectively. A receiver spacing of 3 m was used in order to avoid spatial aliasing of surface waves. Source lines A and B were shot separately along the respective receiver lines A and B, and have 248 and 228 shots, respectively. Sources within the receiver spread were positioned at an interval of 6 m, while source points outside the receiver line were positioned irregularly. The maximum source-receiver offset corresponding to receiver lines A and B was about 953 m and 776 m, respectively. Figure 15(c) shows the source-receiver layout in Cartesian coordinates.

3.3.2. Data quality. A vibroseis [63] was used to generate the source signal. Figure 16(a) shows a particular source position corresponding to receiver line A overlaid on the topography of the region. Figures 16(b) and (d) show the time-domain signature of one vibroseis sweep (source signal) and the corresponding spectrogram. Each sweep is fixed in amplitude in the frequency domain and increases in frequency with increasing time of the sweep. Sweeps are limited in frequency from 7 to 100 Hz. For smooth operation of the vibroseis a 10% cosine taper was applied to the start and the end of a sweep. Hence, a maximum vertical force of 1200 N was only realized in the frequency band 12 to 95 Hz. At each source point, six such sweeps were injected in order to obtain a diversity stack[8], thereby improving the signal to noise ratio.

Figure 16(c) shows the signal recorded by one of the receivers which is about 100 m away from the source point. P-waves propagating directly between the source and receiver are observed as the first burst of energy in the trace. These waves arrive at the receiver within 0.1 s after the shot is fired, hence propagating with speeds between 1 and 2 km s^{-1}. Rayleigh waves

[8] A stack or sum of the signals recorded by a receiver corresponding to multiple sweeps injected at a particular source location aimed at reducing contributions from unwanted local sources of noise.

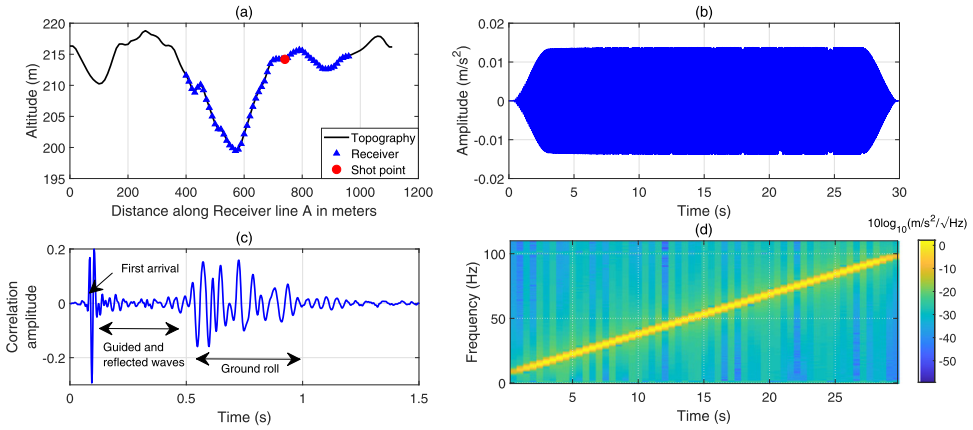

Figure 16. (a) A split-spread source-receiver layout plotted on the topography of the site corresponding to shot number 65. (b) Time signature of a sweep. (c) Signal obtained by cross-correlating the source sweep and the signal recorded at a source-receiver offset of 100 m. The different types of waves recorded by the receiver are shown. (d) Spectrogram of the source-sweep computed with a time resolution of 1 s with a 50% overlap between successive windows.

are observed in the seismogram between 0.5 and 1.0 s and propagate with speeds between 100 and 200 m s^{-1}. The signals that are reflected back to the surface from different subsurface layers occur between 0.2 and 0.5 s and suffer from weak signal over noise ratios.

To give an impression of the seismic data quality we show a shot gather corresponding to a split-spread source-receiver geometry (receivers positioned on either side of the shot point). A raw shot gather is shown in figure 17(a). It corresponds to the source-receiver configuration shown in figure 16(a). Each vertical curve represents the ground response measured at that particular source-receiver separation. As mentioned earlier, the first arrival in the shot gather is the direct P-wave propagating with speeds between 1 and 2 km s^{-1}. Along the time axis the direct arrival is followed by the arrival of several wave-trains that are parallel to the direct arrival and hence propagate with the same velocity as the direct P-waves. These are the guided waves, that can be visualized as leaky modes and appear due to multiple reflections between the unconsolidated top soil and the hard rock. Since the geology in the region is characterized by a transition from soft soil to hard rock at depths between 15 and 40 m, the presence of guided waves is expected. Reflection events which ideally appear as hyperbolas in the time-offset domain are not observed, or are obscured by the guided waves.

Figure 17(b) shows the f-k transform of the raw shot gather. Ground roll and direct arrivals appear in the f-k transformed data as events with a constant slope. Ground roll has a smaller slope in the f-k domain as it has low propagation speeds. The direct waves are the ones that are characterized by a greater slope in the f-k domain and they encompass the outer edges of what is called the 'signal cone' (shown in figure 17(b)). If strong seismic reflections are present in the data, then they should be visible within this cone. Since reflections propagate almost vertically up, they appear as waves propagating with high apparent velocities in the time-offset domain. In our case we observe that the presence of guided waves obscures the reflected waves. Hence, we proceed with a refraction tomography analysis which makes use of the first arrival phases in the seismograms and allows to estimate a P-wave model of the shallow subsurface.

3.3.3. Refraction tomography. There are three major steps that need to be implemented when performing refraction tomography. The first step is the selection of first-arrival times from each

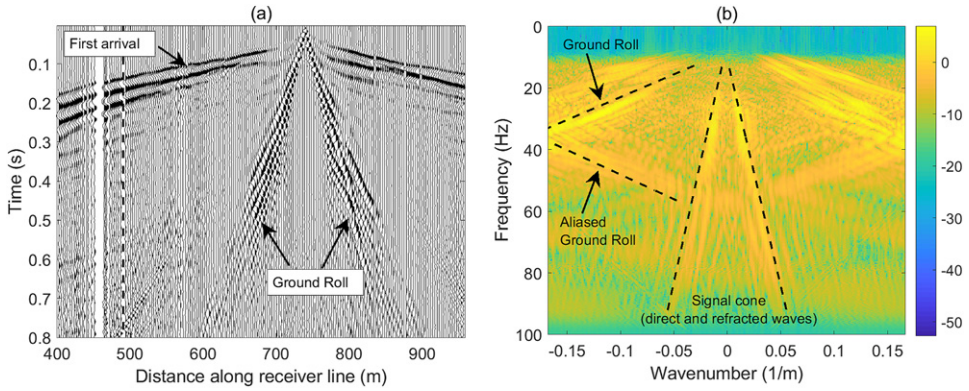

Figure 17. (a) Raw shot gather. Direct and refracted waves constitute the first waves arriving at the receivers, while surface waves, also known as ground roll, are the slowest. Guided waves are visible between 0.2 and 0.3 s (b) f-k transform of the raw shot gather. The ground roll is characterized by a gentle slope in the f-k domain; its aliased part is visible at frequencies greater than 40 Hz. The signal cone representative of subsurface reflection events is encompassed by the direct and refracted P-waves which appear as straight lines with greater f-k slope compared to the ground roll.

of the shot gathers. The selection scheme is based on computing the modified energy ratio of each trace in the shot gather. This approach has been successfully used in the geophysics community to detect the arrival time of P-waves from earthquakes [64]. The second step in the refraction tomography method involves the computation of the theoretical time for the fastest wave traveling between source and receiver. General ray-tracing schemes [65] between source and receiver do not account for the finite frequency effects of wave propagation and the structures present in the vicinity of the ray. Furthermore, we need to account for the band-limited nature of the source signal. The Fresnel volume approach [66] to computing the source-receiver travel-times has the advantage of accounting for effects such as shadow zones and multipathing that are not modeled by mathematical rays [67]. The wavepath Eikonal tomography (WET) method [68] forward models the travel-times by solving the Eikonal equation

$$\left(\frac{\partial T}{\partial x}\right)^2 + \left(\frac{\partial T}{\partial z}\right)^2 = s^2(x,z), \tag{3.2}$$

where $T(x,z)$ represents the first arrival time for the seismic energy propagating between source and receiver and $s(x,z)$ the slowness distribution of the medium. We follow the finite difference scheme proposed by [69] for computing the theoretical first-arrival times. The third and final step in refraction tomography involves the back-projection of travel-time residuals along the previously computed Fresnel volumes. The method for computing the partial derivative of the phase-misfit function with respect to the slowness parameter can be found in [68]. The slowness field is updated iteratively until the rms travel-time error between the modeled and the observed travel-times converges. The numerical stability of this method when applied on synthetic and crosswell data[9] has been discussed in detail in [68]. The results of the WET analysis are shown in figure 18.

[9] Seismic data recorded by receivers positioned at different depths inside a borehole corresponding to source signals injected at different depths inside an adjacent borehole.

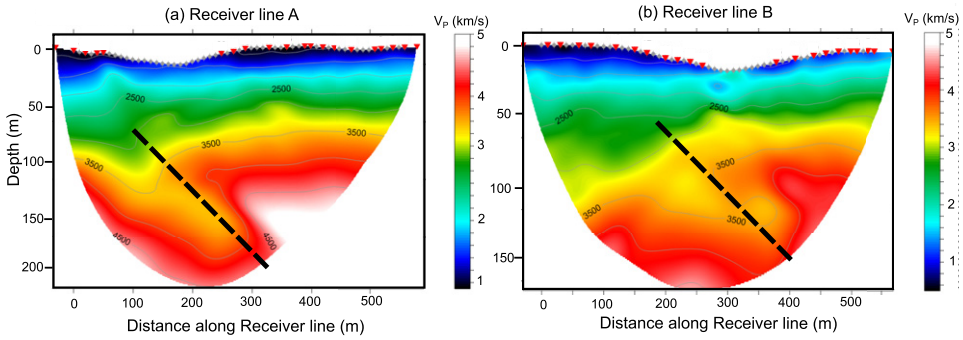

Figure 18. (a) WET P-wave velocity model for receiver line A. (b) WET P-wave velocity model for receiver line B. The dashed lines show the expected dip of the overthrust fault.

Figure 18(a) and (b) show the P-wave velocity distribution in the subsurface corresponding to receiver line A and B, respectively. An overthrust fault[10] in the subsurface is visible beyond depths of 50 m. The black-dashed line shows the dip of the overthrust fault. The increase in the bedrock depth north of receiver line A is more pronounced and can be seen in the P-wave velocity images corresponding to receiver line B. The fault-plane for both lines shows a similar dip and ensures lateral continuity between the two velocity profiles. Note that receiver lines A and B are parallel to each other and that receiver line B is shifted by about 150 m north of receiver line A. The rms of the travel-time residual for receiver line B was higher (2.2 ms) than that observed for A (1.7 ms). Consequently the image resolution of figure 18(b) is smaller than that of figure 18(a). Accurate identification and imaging of such subsurface faults is important to minimize risk in construction of boreholes, caverns and tunnels. This will be addressed in future site assessment studies for Einstein Telescope. Faults deter rock quality, and may introduce instability and water ingress, and should be avoided in the construction of a corner station with its large caverns. While overthrust faults are less of a concern in that regard, the presence of overthrust faults between 40 and 150 m would lead to alternating bands of subsurface material, and this may affect the attenuation properties of the site. For the same reason, constructing corner stations for Einstein Telescope at places where the hard-rock is exposed at the surface is not recommended, and a soft-soil layer over hard-rock is preferred.

Figure 19(a) shows a comparison of the P-wave velocity models derived with the different methods. P-wave models obtained for array B (red) are in reasonable agreement with the P-wave velocities obtained from the borehole (black). However, the P-wave velocity model obtained from array A (blue curve) shows smaller values at shallow depths. This may be because we did not have Rayleigh-wave ellipticity values to constrain the inversion of array A data. Hence, for the theoretical analysis presented in the next section, we use the subsurface model obtained for array B. Figures 19(b) and (c) show the S-wave velocity and the density models derived from the Rayleigh-wave phase-velocity inversion of the data obtained with array A and B, respectively.

[10] A geological feature in which one side of the subsurface rock appears to have been pushed upward due to tectonic activities.

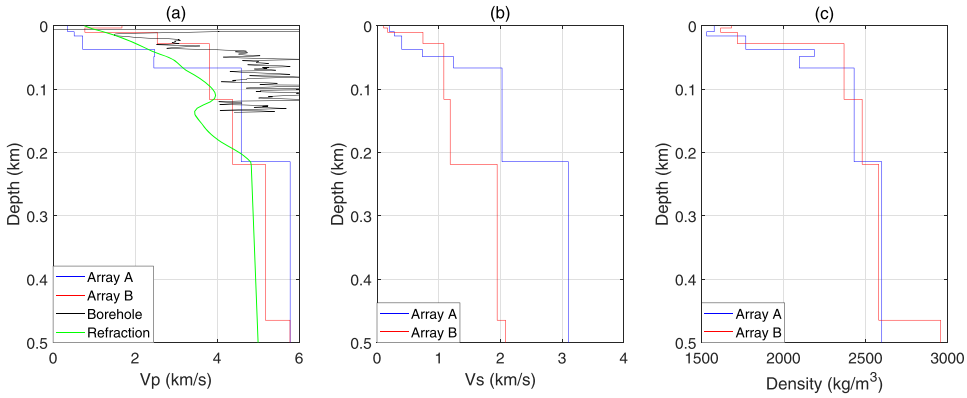

Figure 19. (a) The blue and the red curves show the P-wave velocity models derived with a Rayleigh-wave analysis of data from array A and B, respectively. The green curve corresponds to the P-wave velocity model obtained from refraction tomography of active data acquired along receiver line A and for a source-receiver offset of 300 m. The black curve shows the P-wave velocity model obtained from sonic logging in Borehole A. (b) S-wave velocity models obtained from Rayleigh-wave phase-velocity inversion for array A and B data, respectively. (c) Same as (b), but for the density.

4. Noise interpretation

4.1. Seismic noise attenuation

The geology at Terziet is well suited to attenuate seismic noise created on the surface. In order to understand the factors affecting the attenuation with depth, we determine the surface and the borehole seismic-noise PSD during day- and night-hours separately. Hours between 6 AM and 8 PM CET are treated as daytime, while the rest is treated as night-time. Seismic-noise PSDs were generated for every one-hour of data and the analysis period was from Nov. 2019 to Oct. 2020. Figure 20(a) shows the horizontal component of the seismic noise measured on the surface and underground for both day- and night-time. Between 1 and 4 Hz, the surface seismic-noise PSD increases with frequency and the night-time PSD is about a factor 2 to 5 smaller than that measured during the day. This is because the low-frequency band of the noise is dominated by seismic sources that are in the far field. Far-away sources are characterized by a stationary phase, unlike local sources which are transients. Due to the stationarity of these far-away sources, their contribution to the low-frequency band ($<$4 Hz) is approximately the same for day- and night-time. The slight reduction during night-time is due to the absence of noise sources which are local and broadband in nature and mostly present at daytime. On the contrary the day-night variation of the PSD between 4 and 15 Hz increases drastically by a factor of about 10 to 50. The large difference between day- and night-time PSD in this frequency band is due to the dominant contribution of local anthropogenic noise sources during daytime.

A similar analysis of the day-night variation of the underground seismic-noise PSD is performed. Figure 20(a) shows the horizontal seismic-noise PSD measured in the borehole. Unlike the surface observations, the borehole PSD during daytime is only a factor 2 to 3 higher in the frequency band 1 to 4 Hz, and a factor 3 to 5 higher for frequencies greater than 4 Hz. Although the day-night variation of seismic noise in the borehole is comparable to that measured on the surface for low frequencies, the high-frequency band is significantly different. This is because the high-frequency seismic noise on the surface is dominated by surface waves. These

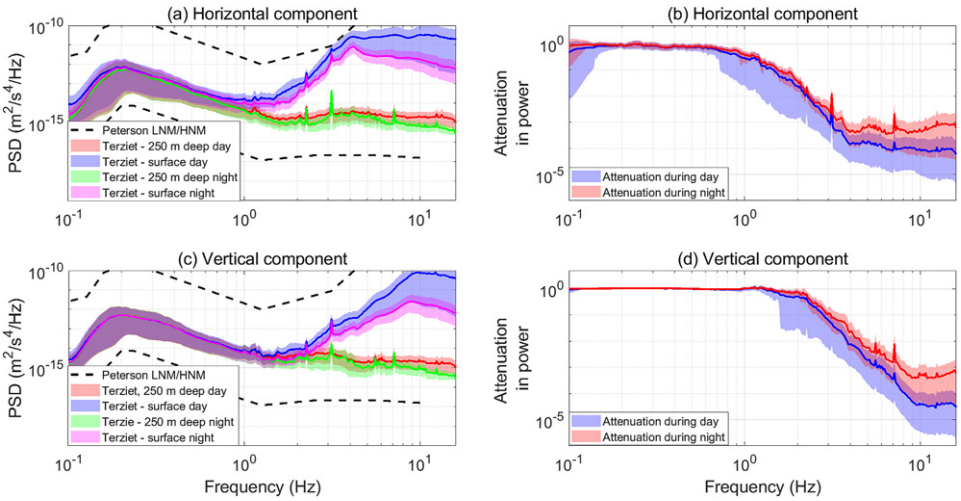

Figure 20. (a) The blue and magenta curves show the mean horizontal component of the seismic noise PSD measured on the surface corresponding to day- and night-hours, respectively, while the red and green curves show the PSD measured underground corresponding to day- and night-hours, respectively. (b) The blue and red curves show the attenuation in seismic noise power ($\frac{\text{borehole}}{\text{surface}}$) during day and night, respectively. The shaded regions show the 10th and the 90th percentile of the estimates for a year of measurement (Nov. 2019–Oct. 2020). (c) and (d) Same as above, but for the vertical component.

high-frequency surface waves due to their smaller wavelength suffer strong attenuation with depth, whereas the low-frequency surface waves are characterized by larger wavelength and attenuate less strongly with depth. Figure 20(c) shows the behavior of the vertical seismic-noise PSD measured on the surface and in the borehole. It is seen that the surface PSD reaches a plateau at about 9 Hz.

Next, the PSD measured on the surface and underground are used to determine the attenuation of seismic noise when going to 250 m depth; this is done separately for day- and night-time. Figure 20(b) shows the attenuation of horizontal seismic-noise power. The attenuation increases with frequency between 1 and 4 Hz and then stabilizes to a constant level of about 10^4 in power for higher frequencies. The modest attenuation at low frequency is due to the strong contribution of surface waves to both the surface and the underground noise. It is also observed that for low frequencies the attenuation during day- and night-time is almost similar, which is expected for the contribution of far-away noise sources. For frequencies greater than 4 Hz, the relative contribution of body waves originating from local and far-way sources to the underground noise increases and hence a flat trend in the attenuation curves is observed. A smaller attenuation during the night in this frequency band can be explained by the absence of local sources of body waves and by the fact that the underground noise spectrum is dominated by distant body-wave sources of noise, which we will refer to as the 'body-wave background'. Unlike the horizontal noise attenuation curve, the vertical noise attenuation shows a continuous increase up to frequencies as high as 9 Hz (see figure 20(d)). This implies that the vertical component of underground seismic noise is impacted by surface waves up to this frequency.

In this context it is important to recall that the presence of higher-order modes of Rayleigh waves at the site has been established already by the analysis of the surface-array measurements discussed in section 2.3. Although the fundamental mode of high-frequency surface waves is

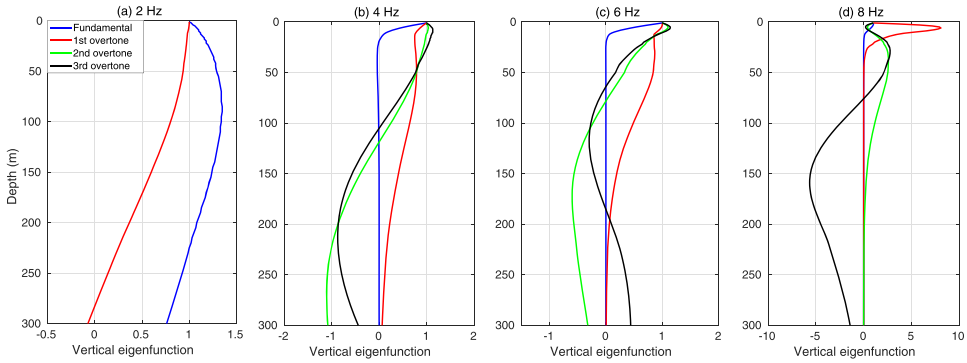

Figure 21. Vertical component of Rayleigh-wave eigenfunctions corresponding to the different modes plotted as function of depth at frequencies, (a) 2 Hz, (b) 4 Hz, (c) 6 Hz and (d) 8 Hz. At higher frequencies, higher-order Rayleigh-wave modes contribute more to the underground seismic noise as compared to the fundamental mode.

expected to attenuate strongly at depth, the higher-order modes suffer less attenuation and these higher-order modes contribute to the underground seismic noise alongside body waves.

To understand the contribution of fundamental and higher-order modes, we compute the surface-wave eigenfunctions as a function of depth. Figure 21 shows the vertical Rayleigh-wave eigenfunctions for various frequencies and different modes. These eigenfunctions describe the (relative) amplitude of the surface wave as a function of depth. They clearly show that the fundamental mode tends to attenuate more rapidly than higher modes. The beams in figures 4 and 5 show that higher modes are excited and we must consider that these can have an impact on the noise at depth, albeit with lower amplitude. However, there is only evidence for at most two higher modes in the data, over a limited frequency band. Eigenfunctions computed for Rayleigh waves comprise the vertical and the radial component, whereas for Love waves only the radial component is relevant. This allows us to obtain a prediction for surface-wave attenuation by taking the ratio between these eigenfunctions at the surface and at a depth of 250 m. A similar approach to understanding the underground seismic noise has been used in [72]. We use the subsurface model derived for array B (section 3.2) to compute the surface-wave eigenfunctions [73], since the borehole is located beneath array B.

Figure 22(a) shows that the fundamental mode of Rayleigh-wave amplitude attenuation is in good agreement with the observed attenuation for frequencies less than 2 Hz. Between 2.5 and 5.0 Hz, the first overtone of the Rayleigh wave dominates the underground spectrum since the observed attenuation in figure 22(a) is in agreement with the theoretical Rayleigh-wave attenuation corresponding to the first overtone. The measured attenuation between 5 and 7.5 Hz can be partly explained by a contribution of the second Rayleigh-wave overtone. The behavior at frequencies above 7.5 Hz, but also in the range 3 to 4 Hz, may point to mixing of wave types.

Figures 22(b) and (c) show the observed attenuation for the horizontal component compared to the calculated Rayleigh- and Love-wave attenuation, respectively. Noise in the low-frequency band between 0.1 and 3.0 Hz can be explained by the theoretical Love-wave attenuation curves shown in figure 22(c). Mixing of surface-wave types and body waves may explain the measured attenuation up to 8 Hz. For frequencies greater than 8 Hz, the observed attenuation cannot be explained by the theoretical surface-wave attenuation curves. Hence, the underground noise for frequencies above 8 Hz may be due to body waves.

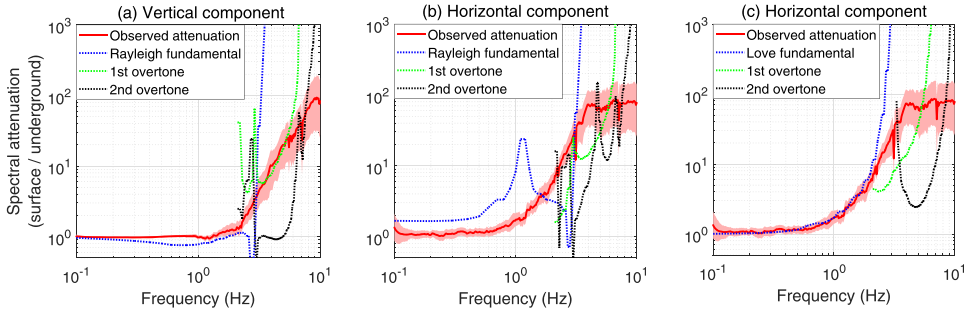

Figure 22. (a) The blue, green, and the black dotted curves show the theoretical vertical-component Rayleigh-wave amplitude attenuation at a depth of 250 m corresponding to the fundamental mode, the first overtone and the second overtone, respectively. The red curve shows the observed attenuation and the red-shaded region represents the 10th and the 90th percentiles. (b) Same as (a), but for the Rayleigh-wave attenuation of the horizontal component. (c) Same as (b) but corresponding to Love-wave attenuation.

4.2. Surface- and body-wave contributions to underground seismic noise

Studies of the contribution of surface and body waves to the underground noise spectra have been of much interest since the 1960s. Pioneering works by [70, 71] have shown useful application of cross-correlating records measured simultaneously on the surface and underground to decipher the wave content in the underground seismic noise. We apply a similar strategy of cross-correlating the surface and the borehole seismic noise. Cross-correlations are computed for every hour of data and averaged over all such windows over a period of one year. The time-domain cross-correlations are then bandpass filtered in small frequency bins.

For surface waves, both the fundamental and excited higher-order modes propagate horizontally along the surface of the Earth. Hence, cross-correlation of data measured by a seismometer on the surface and by a borehole seismometer placed vertically beneath it, will in the case of surface waves result in a cross-correlation time series with maximum energy at zero time-lag. On the contrary, background-body waves can impinge on the two seismometers from random angles and hence will show maximum energy in the cross-correlation time series at a time-lag corresponding to the dominant P or S-wave travel-time between the seismometers. However, a slight ambiguity in the interpretation occurs for horizontally propagating body waves which would also yield maximum cross-correlation at zero time-lag. Similarly, upward-traveling body waves that reflect from the surface will cause standing-wave patterns. This body-wave contribution will also manifest itself at zero time-lag. Thus while a maximum cross-correlation value at a non-zero time-lag indicates the presence of ambient body waves, the reverse is not true: a maximum at zero time-lag does not necessarily imply that body waves do not contribute.

Figure 23 shows the cross-correlation time series between the surface and the borehole sensor for the vertical-component seismic noise data. For the sake of interpretation, the cross-correlations are filtered in twelve frequency bins from 0.1 to 11 Hz. The frequency bands between 0.1 and 3.0 Hz show the cross-correlation peaking at zero time-lag as expected for seismic noise from Rayleigh waves. This is also seen in figure 22(a) where the fundamental mode of Rayleigh-wave attenuation matches well the observed attenuation.

However, the cross-correlation time series in the frequency bands 3 to 4 Hz peaks at 0.1, which points to mixing of body waves and the first overtone of Rayleigh waves. The theoretical P and S-wave up-hole travel-times based on the theoretical subsurface models at the site are 0.075 s and 0.3 s, respectively. From figure 22(a) we inferred that between 5 and 7.5 Hz the

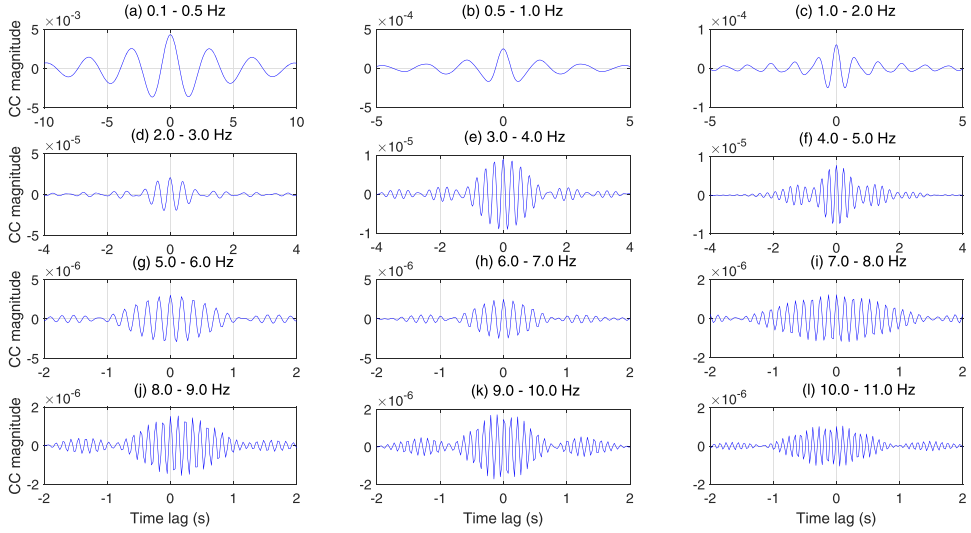

Figure 23. Time-domain cross-correlations of the vertical component of seismic velocity between surface and underground seismometers bandpass filtered in frequency bands, (a) 0.1–0.5 Hz, (b) 0.5–1.0 Hz, (c) 1.0–2.0 Hz, (d) 2.0–3.0 Hz, (e) 3.0–4.0 Hz, (f) 4.0–5.0 Hz, (g) (a) 5.0–6.0 Hz, (h) 6.0–7.0 Hz, (i) 7.0–8.0 Hz, (j) 8.0–9.0 Hz, (k) 9.0–10.0 Hz, and (l) 10.0–11.0 Hz.

attenuation curve may be explained by a contribution from the second Rayleigh-wave overtone. However, besides this second overtone, we can infer the presence of body waves from a shift in the cross-correlation peak in this band by about −0.1 s. For frequencies greater than 8 Hz, the cross-correlation never peaks at zero and lies between 0.075 and 0.2 s of absolute time. This is again due to mixing of P and SV waves. Overall, the peak value of the cross-correlation drops by more than an order of magnitude for frequencies greater than 4.0 Hz as compared to frequencies between 1 and 4 Hz. Although the underground seismic noise comprises higher-order surface-wave modes up to frequencies of about 8 Hz, the reduction in surface-underground correlation is due to the lack of SNR of these surface-wave modes as measured on the surface.

Cross-correlation results for the horizontal component are shown in figure 24. Similar to the vertical component, the horizontal component cross-correlations in the frequency band 0.1 to 3 Hz peaks at zero time and the seismic noise is composed of Love waves. This is shown in figure 22(c) where the observed seismic noise attenuation at a depth of 250 m matches the theoretical Love-wave attenuation. Between 3 and 5 Hz, the cross-correlation peaks between 0.1 s and 0.3 s and reveals a body-wave contribution in the form of SH waves. Similar to the vertical component, cross-correlations reduce by over an order of magnitude for frequencies greater than 4 Hz as compared to the frequency band 1–4 Hz. The cross-correlations in the frequency band 6–7 Hz peaks at zero time and is due to the dominant contribution from the radial component of the second overtone of Rayleigh waves which is shown in figure 22(b). Figures 22(b) and (c) show that for frequencies greater than 8 Hz, the observed attenuation cannot be explained by surface-wave attenuation and we infer a contribution from a body-wave background. This is reinforced by the data shown in figure 24 where for frequencies above 8 Hz the cross-correlations peaks between −0.1 and −0.2 s indicating a clear body-wave contribution.

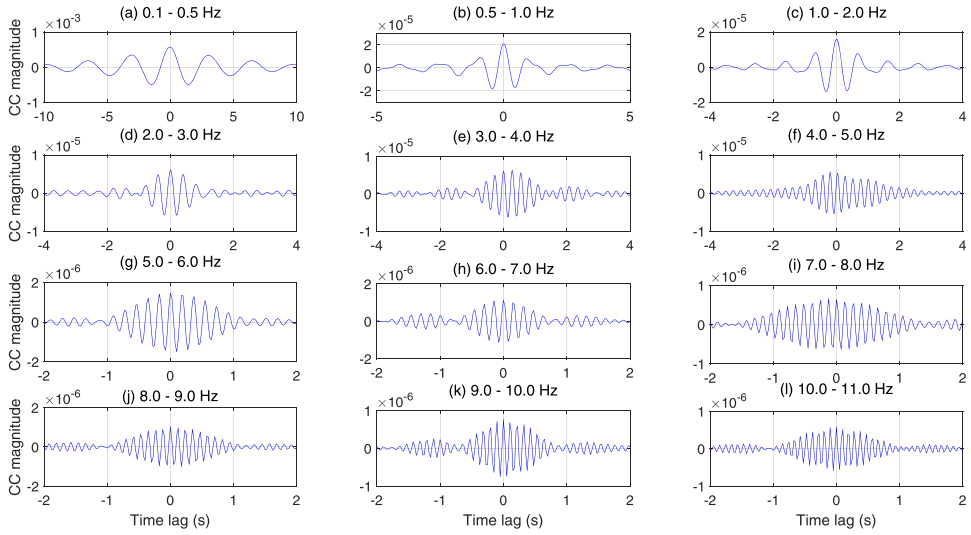

Figure 24. Time-domain cross-correlations of the horizontal component of seismic velocity between surface and underground seismometers bandpass filtered in frequency bands, (a) 0.1–0.5 Hz, (b) 0.5–1.0 Hz, (c) 1.0–2.0 Hz, (d) 2.0–3.0 Hz, (e) 3.0–4.0 Hz, (f) 4.0–5.0 Hz, (g) 5.0–6.0 Hz, (h) 6.0–7.0 Hz, (i) 7.0–8.0 Hz, (j) 8.0–9.0 Hz, (k) 9.0–10.0 Hz, and (l) 10.0–11.0 Hz.

4.3. Body-wave background

Next we use the data to estimate the seismic noise contribution from far-away body-wave sources which we refer to as the 'body-wave background'. We now know that at frequencies greater than 4 Hz the underground seismic noise attenuation is smaller during night-time than during the day. This implies that the underground seismic noise at night is significantly higher than what would be expected if there were only surface waves. Thus we hypothesize that the underground seismic noise $\mathrm{PSD}_{\mathrm{depth}}$ can be expressed as

$$\mathrm{PSD}(f)_{\mathrm{depth}} = \mathrm{PSD}(f)_{\mathrm{surface}}\,\alpha(f) + \beta(f), \tag{4.1}$$

where $\mathrm{PSD}(f)_{\mathrm{surface}}$ denotes the seismic noise on the surface, $\alpha(f)$ the frequency dependent attenuation and $\beta(f)$ the frequency dependent body-wave background noise.

The observed seismic noise on the surface $\mathrm{PSD}(f)_{\mathrm{surface}}$ includes contributions from both surface and body waves. During daytime, the increased power of seismic noise on the surface is sufficiently strong to leave its imprint underground and therefore we observe some degree of diurnal variation in the underground seismic noise. However during the night, due to reduced seismic noise on the surface, the underground seismic environment is sufficiently quiet for the body-wave background to significantly contribute to the total underground seismic noise. In order to estimate the body-wave background from equation (4.1), we need to know the attenuation factor $\alpha(f)$. Assuming that the body-wave background and the attenuation factor do not change between day- and night-time observations, we can solve for $\beta(f)$. Figures 25(a) and (b) show the estimated mean body-wave background corresponding to the horizontal and vertical component of seismic noise, respectively. The body-wave background for frequencies below 4 Hz is a factor 3 to 4 smaller in power compared to the total underground seismic noise. However, at frequencies greater than 4 Hz, the body-wave background contributes about half

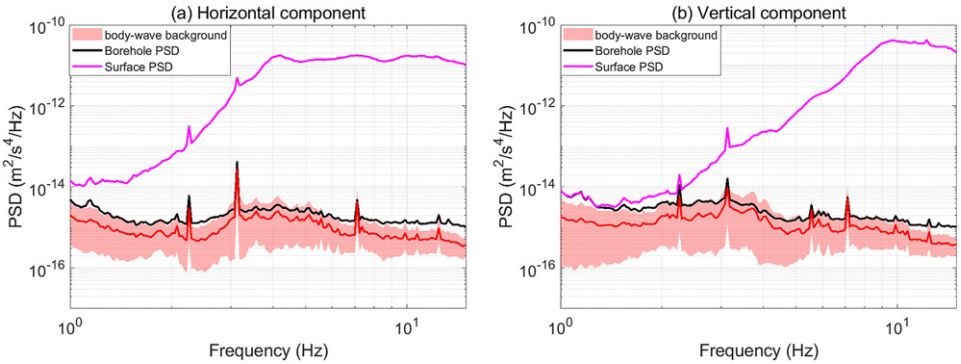

Figure 25. (a) PSD of the body-wave background corresponding to the horizontal component of seismic noise. The magenta and black curves correspond to seismic noise measured on the surface and underground, respectively. The shaded region shows the 10th and 90th percentiles over all analysis windows. (b) Same as (a) but for the vertical component.

of the total underground seismic noise power. Moreover, this implies that constructing Einstein Telescope at greater depth will not significantly improve its performance with respect to this contribution.

5. Discussion and conclusions

We presented a detailed characterization of surface and underground seismic noise measured at Terziet in Limburg, situated in a rural area in the southernmost tip of The Netherlands between Germany and Belgium. This Euregio Meuse–Rhine site has several important advantages for hosting Einstein Telescope. Firstly the site is in a rural area designated as a 'quiet zone' and features moderate anthropogenic seismic noise levels. Moreover we demonstrated that the presence of a hard-rock Carboniferous basement with an overburden of less consolidated Cretaceous/Pleistocene soft-soil is effective in minimizing underground seismic noise. The characteristic geology is efficient in attenuating seismic noise power generated locally at the surface by about a factor 10^4 when going at 250 m depth and has relatively low levels of ambient background noise.

Furthermore, it was demonstrated that this geology will be effective in suppressing Newtonian noise generated by surface waves [44]. This can be understood as follows. Firstly, the impedance differences of the various layers lead to reflections at the layer-interfaces, in this way attenuating the seismic energy that is generated at the surface. This causes the seismic-noise power to be constrained to the near-surface soil layers, with only a small fraction of noise power reaching locations near the sensitive test masses. Secondly, the seismic waves near the surface are mostly Rayleigh and Love waves which are highly dispersive and have short wavelengths in the soft-soil layers. These waves attenuate strongly with depth, and at high frequency, these horizontally traveling waves attenuate even more strongly due to anelastic effects.

When calculating Newtonian noise not only the seismic PSD values, but also the wavelengths are important. These surface waves have relatively short wavelengths, and this leads to cancellation effects when summing the Newtonian noise on a test mass over kilometer-scale integration bounds. Thirdly, the seismic waves will have high velocity in the deep hard-rock

layers and will consequently have lower amplitudes. This causes underground tunnel and cavern walls to experience relatively small displacements, leading to low associated Newtonian noise contributions from nearby structures. Taking all these effects into account it has been shown that the site's geology, featuring soft-soil layers on hard-rock, is effective in attenuating Newtonian noise from surface waves below the sensitivity required for Einstein Telescope [44].

Seismic noise measurements were performed with an array of seismometers installed on the surface. Beamforming was used to extract the propagation modes of the ambient seismic noise and the Rayleigh-wave dispersion in the region. The fundamental Rayleigh-wave mode dominates the vertical component of surface seismic noise up to frequencies of 5 Hz. While the first Rayleigh-wave overtone and the fundamental mode were found to contribute equally in the band 5–8 Hz, a weak second Rayleigh-wave overtone was observed for frequencies greater than 10 Hz. The absence of the first overtone in the frequency band below 5 Hz and of the second overtone below 10 Hz can be due to two factors. Either the source mechanism generating the noise does not significantly excite the higher-order modes at these frequencies, or the propagation velocities of these modes are too high for the surface array to resolve. The latter may also be the reason why P-waves are not delineated in the beamforming analysis.

P-wave velocities at the site range between 1.5 to 2 km s^{-1} near the surface. Hence, beamforming of the vertical-component surface seismic noise provides information about the Rayleigh-wave propagation modes and their velocities. Consequently, understanding the local body- and surface-wave contributions could only be done by inferring the HVSR and the ellipticity on the surface from the three-component single-station data. Such methods give a qualitative understanding of the wave types, because the horizontal component is composed of SH, Love and Rayleigh waves and the vertical component is composed of P, SV and Rayleigh waves. Determining the exact contribution by Rayleigh waves and body waves (P and SV) on the vertical component of the seismic noise is possible by using a large-aperture surface-array of seismometers which can resolve the travel-times between the fast propagating body waves and the more slowly propagating surface waves.

We only performed vertical-component array measurements and this limits our understanding of the Love-wave content. Hence, an array of tri-axial seismometers should be deployed at the site to gain a better understanding of the Love- and SH-wave contributions.

We could qualitatively comment on the surface- and body-wave contributions by using a cross-correlation analysis of the surface and underground seismic noise. Computation of the surface-wave eigenfunctions was useful to determine the theoretical attenuation of surface waves when going underground. Overall, we conclude that the band 0.1–3 Hz is dominated by Rayleigh waves in the vertical component and by Love waves in the horizontal component of the noise. This applies to both surface and underground seismic noise. The frequency band 3–5 Hz shows a significant contribution by SH waves to the horizontal component of the surface and underground seismic noise. The same was observed for the vertical component, although the first Rayleigh-wave overtone was found to be present in the underground seismic noise. In the frequency band 5–7 Hz, the underground vertical component noise has a contribution from the second Rayleigh-wave overtone besides body waves. For frequencies greater than 7 Hz, the contribution of surface waves is smaller and it is almost absent for frequencies greater than 8 Hz. This explains the flat trend in the attenuation curve. Similar trends were observed for the horizontal component of the underground seismic noise, and above 7 Hz the noise is dominated by SH waves.

While low-frequency surface waves generated by both local and far-away sources are significantly attenuated while going underground, local and far-away generated body-waves are not attenuated as much. Analysis of PSDs simultaneously recorded at the surface and in the

borehole suggests that for frequencies above 4 Hz approximately 50% of the subsurface noise consists of body-wave background (far-away sources). The low level of seismic noise at the depth of the detector may still limit its sensitivity and we may need to predict and subtract the resulting Newtonian noise. This requires the availability of a detailed model of subsurface parameters, such as its P-wave and S-wave velocity and attenuation properties. The passive surface-wave measurements are used to derive shear velocities and attenuation properties. Subsurface models sensitive up to 300 m depth were derived by using the Rayleigh-wave dispersion. In addition, an active seismic survey was carried out to derive P-wave velocities. Wavepath Eikonal tomography was used on the source-receiver refracted wave travel-times to obtain a subsurface model accurate to a depth of about 200 m. An initial one-dimensional subsurface model was derived that allows to predict first-order seismic noise effects on a potential underground gravitational-wave detector in Terziet. Our results confirm the suitability of Terziet as a potential site for Einstein Telescope.

Future work should be directed at a better understanding of body-wave contributions to the subsurface noise to allow improved predictions of the Newtonian noise contribution to the sensitivity of Einstein Telescope. Such understanding could be gained from deploying a larger aperture array at the surface featuring sensors measuring all three displacement components.

Acknowledgments

This work is part of the research program 'Advanced Virgo—Probing the dynamics of spacetime' with Project Number 680-45-113, which is (partly) financed by the Dutch Research Council (NWO), and Shell-NWO/FOM Computational Sciences for Energy Research (CSER), Project No. 12CSER075. Moreover we thank NWO for the funding provided within the SENSEIS project: 'STW Open Technology Program, Project 13338'.

Data availability statement

The data that support the findings of this study are available upon reasonable request from the authors.

ORCID iDs

Soumen Koley https://orcid.org/0000-0002-5793-6665
Jo van den Brand https://orcid.org/0000-0003-4434-5353
Xander Campman https://orcid.org/0000-0001-6482-1391

References

[1] Buikema A *et al* 2020 *Phys. Rev.* D **102** 062003
[2] Abbott R *et al* 2021 *Phys. Rev.* X **11** 021053
[3] Punturo M *et al* 2010 *Class. Quantum Grav.* **27** 194002
[4] Hall E D *et al* 2021 *Phys. Rev.* D **103** 122004
[5] van den Brand J 2019 *100 Years of General Relativity: Advanced Interferometric Gravitational-Wave Detectors* vol 5 (Singapore: World Scientific) p 1
[6] Hild S *et al* 2011 *Class. Quantum Grav.* **28** 094013
[7] Hughes S A and Thorne K S 1998 *Phys. Rev.* D **58** 122002

[8] Fiorucci D, Harms J, Barsuglia M, Fiori I and Paoletti F 2018 *Phys. Rev.* D **97** 062003
[9] Aasi J *et al* 2015 *Class. Quantum Grav.* **32** 074001
[10] Acernese F *et al* 2014 *Class. Quantum Grav.* **32** 024001
[11] Boschi V 2019 *J. Acoust. Soc. Am.* **145** 1668
[12] Acernese F *et al* 2010 *Astropart. Phys.* **33** 182–9
[13] Amann F *et al* 2020 *Rev. Sci. Instrum.* **91** 094504
[14] Bonnefoy-Claudet S, Cotton F and Bard P-Y 2006 *Earth-Sci. Rev.* **79** 205–27
[15] Koper K D, Seats K and Benz H 2010 *Bull. Seismol. Soc. Am.* **100** 606–17
[16] Harmon N, Gerstoft P, Rychert C A, Abers G A, Salas de La Cruz M and Fischer K M 2008 *Geophys. Res. Lett.* **35**
[17] Brooks L A, Townend J, Gerstoft P, Bannister S and Carter L 2009 *Geophys. Res. Lett.* **36** 23
[18] Koley S, Bulten H J, van den Brand J, Bader M, Campman X and Beker M 2017 S-wave velocity model estimation using ambient seismic noise at Virgo, Italy *SEG Technical Program Expanded Abstracts 2017* (Society of Exploration Geophysicists) pp 2946–50
[19] Lacoss R T, Kelly E J and Toksöz M N 1969 *Geophysics* **34** 21–38
[20] Campillo M and Paul A 2003 *Science* **299** 547–9
[21] Shapiro N M and Campillo M 2004 *Geophys. Res. Lett.* **31** 7
[22] Gouédard P *et al* 2008 *Geophys. Prospect.* **56** 375–93
[23] Yao H, Beghein C and Van Der Hilst R D 2008 *Geophys. J. Int.* **173** 205–19
[24] Kimman W P, Campman X and Trampert J 2012 *Bull. Seismol. Soc. Am.* **102** 1388–99
[25] Hannemann K, Papazachos C, Ohrnberger M, Savvaidis A, Anthymidis M and Lontsi A M 2014 *J. Geophys. Res. Solid Earth* **119** 4979–99
[26] Wang K, Luo Y and Yang Y 2016 *Geophys. J. Int.* **205** 715–27
[27] Wathelet M, Jongmans D and Ohrnberger M 2004 *Near Surf. Geophys.* **2** 211–21
[28] Ellis D V and Singer J M 2007 *Well Logging for Earth Scientists* vol 692 (Dordrecht: Springer)
[29] Dunkin J W 1965 *Bull. Seismol. Soc. Am.* **55** 335–58
[30] Roth M, Holliger K and Green A G 1998 *Geophys. Res. Lett.* **25** 1071–4
[31] Sheehan J R, Doll W E and Mandell W A 2005 *J. Environ. Eng. Geophys.* **10** 21–34
[32] Song Y Y, Castagna J P, Black R A and Knapp R W 1989 Sensitivity of near-surface shear-wave velocity determination from Rayleigh and love waves *SEG Technical Program Expanded Abstracts 1989* (Society of Exploration Geophysicists) pp 509–12
[33] Asten M W and Henstridge J D 1984 *Geophysics* **49** 1828–37
[34] Woods J W and Lintz P R 1973 *Geophysics* **38** 1023–41
[35] Koley S, Bulten H J, van den Brand J, Bader M, Campman X and Beker M 2017 *First Break* **35** 71–8
[36] Mykkeltveit S and Kerr A U 1985 *The VELA Program—A Twenty-Five Year Review of Basic Research* vol 18 (Defence Advanced Research Project Agency) pp 546–53
[37] Welch P 1967 *IEEE Trans. Audio Electroacoust.* **15** 70–3
[38] Peterson J 1993 *US Geol. Surv. Open-File Report* vol 93 (US Geological Survey)
[39] Longuet-Higgins M S 1950 *Phil. Trans. R. Soc.* A **243** 1–35
[40] Foti S *et al* 2018 *Bull. Earthq. Eng.* **16** 2367–420
[41] Merchant B J and Slad G W 2017 Next generation qualification: kinemetrics STS-5A seismometer evaluation *Technical Report* AlbuquerqueSandia National Laboratory (SNL-NM)
[42] Kedar S, Longuet-Higgins M, Webb F, Graham N, Clayton R and Jones C 2008 *Proc. R. Soc.* A **464** 777–93
[43] Stutzmann E, Schimmel M, Patau G and Maggi A 2009 *Geochem. Geophys. Geosyst.* **10** 11
[44] Bader M, Koley S, van den Brand J, Campman X, Bulten H J, Linde F and Vink B 2021 *Class. Quantum Grav.* https://doi.org/10.1088/1361-6382/ac1be4
[45] Acerra C, Havenith H B and Zacharopoulos S 2004 Guidelines for the implementation of the *h/v* spectral ratio technique on ambient vibrations measurements, processing and interpretation *Technical Report* (European Commission)
[46] Konno K and Ohmachi T 1998 *Bull. Seismol. Soc. Am.* **88** 228–41
[47] Hobiger M, Bard P Y, Cornou C and Le Bihan N 2009 *Geophys. Res. Lett.* **36** 14
[48] Trautwein-Bruns U, Schulze K C, Becker S, Kukla P A and Urai J L 2010 *Tectonophysics* **493** 196–211
[49] Hinzen K, Reamer S K, Stein S and Mazzotti S 2007 *Seismicity, Seismotectonics, and Seismic Hazard in the Northern Rhine Area* Special Papers vol 425 (Boulder, Colorado: Geological Society of America) p 225

[50] van Thienen-Visser K and Breunese J N 2015 *Lead. Edge* **34** 664–71
[51] Coughlin M *et al* 2017 *Class. Quantum Grav.* **34** 044004
[52] Schwartz E *et al* 2020 *Class. Quantum Grav.* **37** 235007
[53] Haskell N A 1953 *Bull. Seismol. Soc. Am.* **43** 17–34
[54] Killeen P G 1982 Gamma-ray logging and interpretation *Developments in Geophysical Exploration Methods—3* (Netherlands: Springer) pp 95–150
[55] Brannon H R Jr and Osoba J S 1956 *Trans. AIME* **207** 30–5
[56] Schlumberger C, Schlumberger M and Leonardon E G 1934 *Trans. AIME* **110** 237–72
[57] Thorez J, Streel M, Bouckaert J and Bless M 1977 *Meded. Rijks Geol. Dienst* **28** 17–32
[58] Sambridge M 1999 *Geophys. J. Int.* **138** 479–94
[59] Wathelet M, Jongmans D and Ohrnberger M 2005 *Bull. Seismol. Soc. Am.* **95** 1787–800
[60] Scherbaum F, Hinzen K-G and Ohrnberger M 2003 *Geophys. J. Int.* **152** 597–612
[61] Wright H E, Frey D G *et al* 1965 *Int. Studies on the Quaternary: Papers Prepared on the Occasion of the 7th Congress of the Int. Association for Quaternary Research* vol 84 (Boulder, Colorado 1965) (Geological Society of America)
[62] Bullock S J 1978 *Environ. Eng. Geosci.* **15** 19–35
[63] Baeten G J M 1989 Theoretical and practical aspects of the Vibroseis method *PhD Thesis* TU Delft
[64] Wong J, Han L, Bancroft J and Stewart R 2009 Automatic time-picking of first arrivals on large seismic datasets *CREWES, Univ. Calgary, Calgary, AB, Canada, Tech. Rep* **26** 14
[65] Um J and Thurber C 1987 *Bull. Seismol. Soc. Am.* **77** 972–86
[66] Červenỳ V and Soares J E P 1992 *Geophysics* **57** 902–15
[67] Woodward M J 1992 *Geophysics* **57** 15–26
[68] Schuster G T and Quintus-Bosz A 1993 *Geophysics* **58** 1314–23
[69] Qin F, Luo Y, Olsen K B, Cai W and Schuster G T 1992 *Geophysics* **57** 478–87
[70] Seriff A J, Velzeboer C J and Haase R J 1965 *Geophysics* **30** 1187–90
[71] Douze E J 1967 *Bull. Seismol. Soc. Am.* **57** 55–81
[72] Spica Z J, Nakata N, Liu X, Campman X, Tang Z and Beroza G C 2018 *Seismol. Res. Lett.* **89** 1450–66
[73] Herrmann R B 2013 *Seismol. Res. Lett.* **84** 1081–8